Experimental and numerical study on progressive collapse of composite steel-concrete frames

Jing-Xuan Wang[1,a] , Ya-Jun Shen[2,b], Kan Zhou[*3,a], and Yong Yang[1b]

[1]School of Civil Engineering, Lanzhou University of Technology, Lanzhou 730050, China.
[2]School of Civil Engineering, Dalian University of Technology, Dalian 116024, China
[3]School of Built Environment, Engineering and Computing, Leeds Beckett University, City Campus, Leeds, LS1 3HE, UK

Abstract. This paper presents an experimental investigation into the progressive collapse behavior of composite steel-concrete frames under various column removal scenarios. This study involves testing two two-bay, two-story composite frames featuring CFST columns and profiled steel decking composite slabs. Two removal scenarios, involving the corner column and middle column, are examined. The paper reports on the overall and local failure modes, vertical force-deformation responses, and strain development observed during testing. Findings indicate that structural failure initiates due to fracture and local buckling of the steel beam. Moreover, the collapse resistance and ductility of the middle column removal scenario surpass those of the corner column removal scenario. Subsequent numerical analysis reveals the significant contribution of the composite slab to collapse resistance and capacity. Additionally, it is found that horizontal boundary conditions notably influence the collapse resistance in the middle column removal scenario only. Finally, the paper proposes a simplified calculation method for collapse resistance, which yields satisfactory predictions.
.

Keywords: Steel-concrete composite substructure; progressive collapse; experimental study; mechanism analysis; simplified calculation

1. Introduction

Accidental actions may damage critical members in building structures and therefore may trigger progressive collapse disproportionate to initial damage (ASCE, 2010). Resistance to the progressive collapse of building structures had been covered by GSA 2013, DoD 2016, and CECS392 2021. These codes adopt a column removal approach to study the behavior of the remaining structure. Researchers have studied progressive collapse resistance of beam-column RC and steel substructures by means of experiments, numerical simulation, and theoretical studies (Adam *et al*. 2018). These studies cover progressive collapse resistance of beam-column joints (Zhu *et al*. 2021, Almusallam *et al*. 2018, Campione *et al*. 2021, Lew *et al*. 2013, Ma *et al*. 2019), the influence of various beam-column connection configurations on collapse performance of joints (Chen and Tan. 2020, Al-Salloum *et al*. 2018), the influence of various span ratios (Zhong *et al*. 2020) and influence of section scale and reinforcement detailing on collapse resistance (Meng *et al*. 2021, Almusallam *et al*. 2017). The beam-column joints with equal spans were greater than that of the substructure with unequal spans.

Compared with beam-column joints, single-story planar frames may better reflect the collapse mechanism of the entire structure. Researchers (Yang *et al*. 2016, Guo *et al*. 2021, Yang *et al*. 2021, Kang *et al*. 2017, Demonceau *et al* .2010) studied the collapse mechanism of a single-story frame with various structural forms. The catenary stage

significantly improves the collapse resistance. Moreover, the effect of horizontal boundaries on collapse resistance has been studied. Diao *et al*. (2020) presented three experimental tests on the collapse resistance of RC structures and found that horizontal restraints influenced the collapse resistance of the structures. Qian *et al*. (2020) investigated the progressive collapse of two-story steel sub-frames under symmetrical boundary conditions. The results indicate that both flexural action and catenary action contribute to the resistance in large deformation stage. Pham *et al*. (2017) tested the collapse resistance of a beam-slab structure and found that the specimen with the removal of penultimate column was more vulnerable to progressive collapse. Slabs have been found to play an important role in the collapse resistance (Lu *et al*. 2017). Kong *et al*. (2020) quantified the effect of RC slab on the collapse resistance of a three-dimensional steel structure. They concluded that RC slab significantly contributed to collapse resistance. Wang *et al*. (2019) found that composite slab significantly improved the collapse resistance of steel structure. Adam *et al*. (2020) studied the internal force variation and overall response of a full-scale RC framed structure. The flexural and Vierendeel action have been found to have contributed to the collapse resistance. Zandonini *et al*. (2019) studied the response of concrete slab in a steel-concrete frame and highlighted the necessity of strengthening the constraints between beams and floor slabs.

Current research on progressive collapse resistance of structures mainly focused on RC and steel substructures. For composite framed structures using concrete-filled steel tube (CFST), the study is limited. Existing research mainly focused on CFST column- steel beam joints with different connection configurations (Wang *et al*. 2016, Gao *et al*. 2019, Lu *et al*. 2019). Recently, the research group of the first author has also conducted numerical and experimental studies (Wang *et al*. 2020, Wang *et al* .2020. Wang *et al*

∗Corresponding author, Ph.D., Senior Lecturer
 E-mail: k.zhou@leedsbeckett.ac.uk
[a] Professor
 E-mail: cewangjx@lut.edu.cn
[b] Ph.D. Student

2022) on the progressive collapse resistance and found that structural failure was mainly initiated by steel beam fracture.

Due to the high cost and limitations of test facilities, the majority of existing experimental studies on progressive collapse have been conducted using single-story beam-column substructures. Substructures can represent the local failure behavior of the actual structures. Nonetheless, the study of progressive collapse can also be conducted using large-scale framed structures, enabling the examination of the effects of various column removal scenarios. This paper focuses on two-bay, two-story composite frames as sub-structures and presents an experimental investigation aimed at studying their resistance to progressive collapse. A corner column removal scenario and a middle column removal scenario were considered. Other factors that were considered include: (1) composite slabs, (2) asymmetric horizontal constraint at beam ends, and (3) load applied at

the top of the non-failure columns. Stress and internal force developments are explored to understand collapse resistance. The influence of key factors on collapse resistance is then analyzed using finite element (FE) models. A simplified calculation method for collapse resistance is calculated and validated.

2. Experimental program

2.1 Specimens design

A 12-story composite framed structure was considered. The columns had square CFST cross-sections. The steel section was 600 mm×12 mm in size. The dimensions of the steel beam were 600 mm×300 mm×16 mm×24 mm (overall depth × overall width × web thickness × flange thickness). The test specimens were extracted from this framed structure, as shown in Fig. 1.

| (a) Plan view | (b) Elevation view |

Fig. 1 The prototype structure and test specimen position (unit: mm)
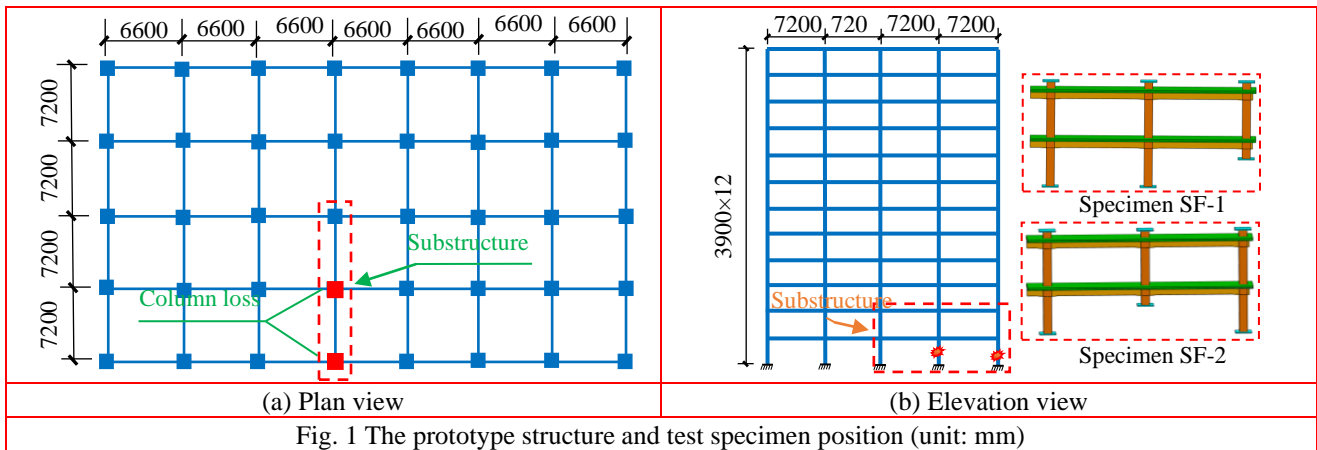
Two test specimens were designed to study the influence of different column removal scenarios. They simulated corner column removal (SF-1) and middle column removal (SF-2), respectively. Given the capacity of the facilities, the substructure was further scaled to a quarter of the prototype structure. The test specimens had a column spacing of 1800mm, and story height of 1000 mm. The dimensions of the steel beam section were H 150×75×4×6 mm. M13 shear studs with a height of 40 mm were arranged in a single row with a spacing of 75mm. The profiled steel decking used was of type YX35-125-750, featuring a thickness of 1 mm, a wave height of 35 mm, a length of 125 mm for each wave, and an effective width of 750 mm. Detailed dimensions are illustrated in Fig. 2a. The characteristic value of cube strength of the concrete in composite slab was 30 MPa. The reinforcement was HPB300 (nominal yield strength of 300 MPa) with a diameter of 6 mm. They were arranged at a transverse spacing of 120 mm, and longitudinal spacing of 150 mm. Details of the beam to columns connection are shown in Fig. 2. Table 1 summarizes the detailed information of the two specimens.
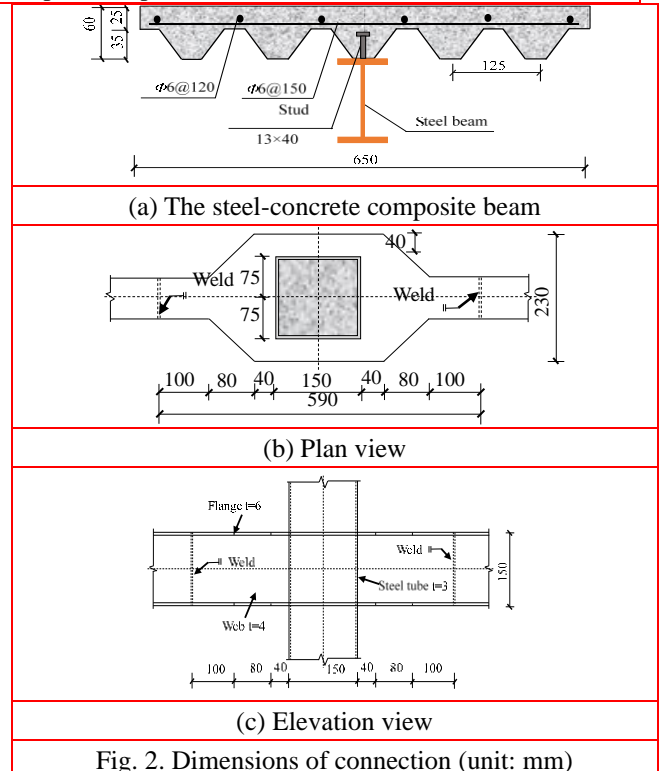

(a) The steel-concrete composite beam

(b) Plan view

(c) Elevation view

Fig. 2. Dimensions of connection (unit: mm)

Table 1 Detailed information of two specimens

Specimen label	CFST column section/mm	Steel beam section/mm	Composite slab/mm		Concrete grade		Steel grade	Removal scenarios
			Width	Thickness	Core concrete	slab		
SF-1	□150×3	H150×75×4×6	650	60	C40	C30	Q235B	Corner column
SF-2	□150×3	H150×75×4×6	650	60	C40	C30	Q235B	Middle column

2.2 Material properties

Results of material properties are shown in Table 2. They were obtained from standard tests according to the Chinese standard GBT228 2002. The cube compressive strengths of core concrete and slab concrete were 30.8 MPa and 25.3 MPa at 28 days, respectively. Concrete strength at test day was not obtained.

Table 2 Mechanical properties of steel

	The measured depth t(mm)	Yield strength of steel f_y(MPa)	Ultimate strength of steel f_u(MPa)	Young's modulus of steel E_s(GPa)	Poisson ratio of steel μ_s	Elongation of steel Δ(%)
Steel tube	2.8	327.5	430.0	2.20	0.289	30.40
Beam flange	5.7	226.0	421.7	2.05	0.306	25.64
Beam Web	3.8	286.7	413.3	1.90	0.290	24.42
Reinforcement	6.0	346.2	580.1	1.90	/	12.27

2.3 Experimental setup and loading procedure

The experimental setup consisted of a vertical reaction frame system, a horizontal reaction frame system, a pressure transducer, and a restraint system, as shown in Fig. 3. A unilateral asymmetric horizontal constraint device was designed, and a tension-compression sensor was employed to measure the horizontal tension force at the beam ends. Axial load was applied on the top of the non-failure columns, and the column load ratio was 0.3. An out-of-plane restraint device was designed to prevent the specimen from lateral deformation. Displacement control was employed to apply load on the damaged column. This was achieved by controlling a hydraulic jack fixed to the portal frame. A pressure sensor was placed on the top of the failure column to measure the vertical reaction force in the structure.

According to the collapse criterion specified in DoD (2016), the vertical displacement of the failure column was set to 360 mm. The loading system was as follows: the first 30 mm was loaded in three stages, each stage being 10 mm, and the speed was 1 mm/min. For the remaining 330mm, loading was applied by displacement at a constant rate of 3 mm/min until the loading scheme was completed.

1. Reaction frame
2. Specimen
3. Restraint device at beam end
4. Out-of-plane restraint device
5. Ground beam
6. Loading beam
7. Load cells
8. M42 bolts
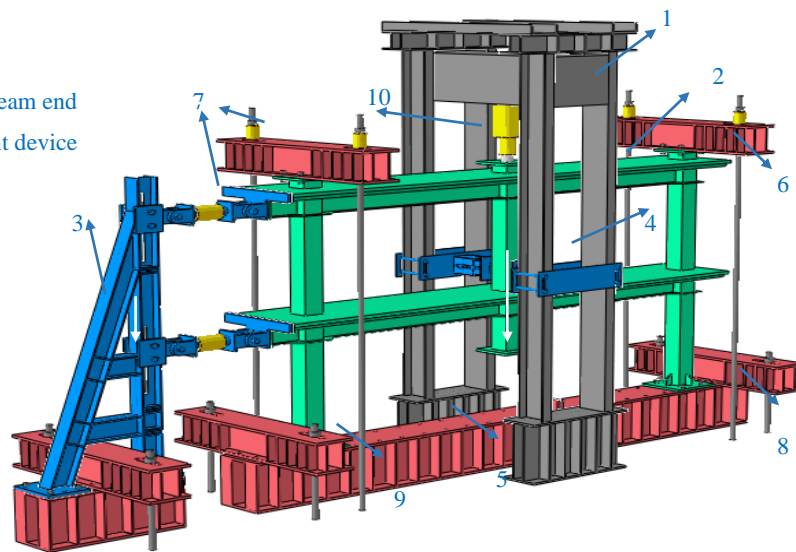9. Anchor bolts
10. Hydraulic jack

Fig. 3 Schematic view of test setup

2.4 Measurement scheme

Fig. 4 shows the arrangement of strain gauges on beam sections for specimen SF-1. These sections were numbered from B1 to B8. In each section, six strain gauges were used, with two arranged on the top flange, web and bottom flange, respectively. The location and number of strain gauges for specimen SF-2 were identical to SF-1. Linear variable differential transformers (LVDT) positioned at the bottom of the failed column C (or B for specimen SF-2) were employed to measure the vertical displacement. Four other LVDTs were placed under the mid-span of the beams to measure the beam deflection.

Fig. 4 Arrangements of strain gauges and LVDTs for SF-1
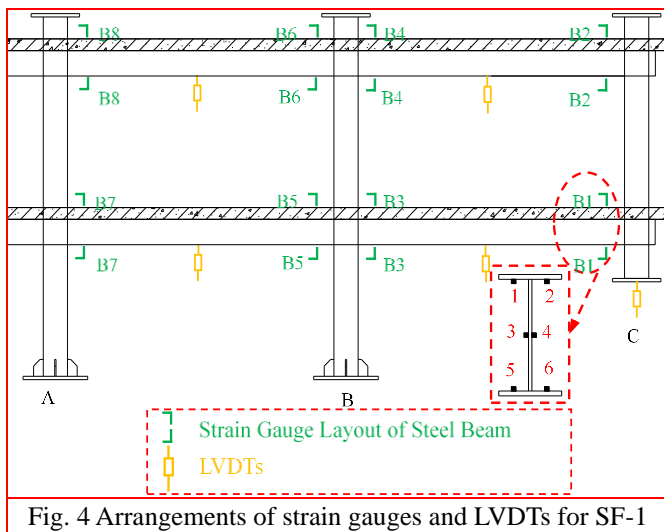
3. Experiment results and discussions
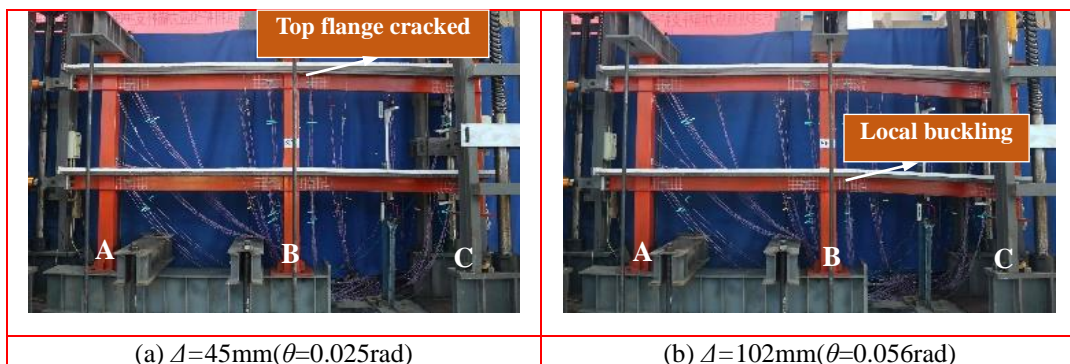
3.1 Experimental failure modes

This section concerns the failure modes of the tests. Overall failure development was reported, followed by local failure modes of steel beams and composite slabs.
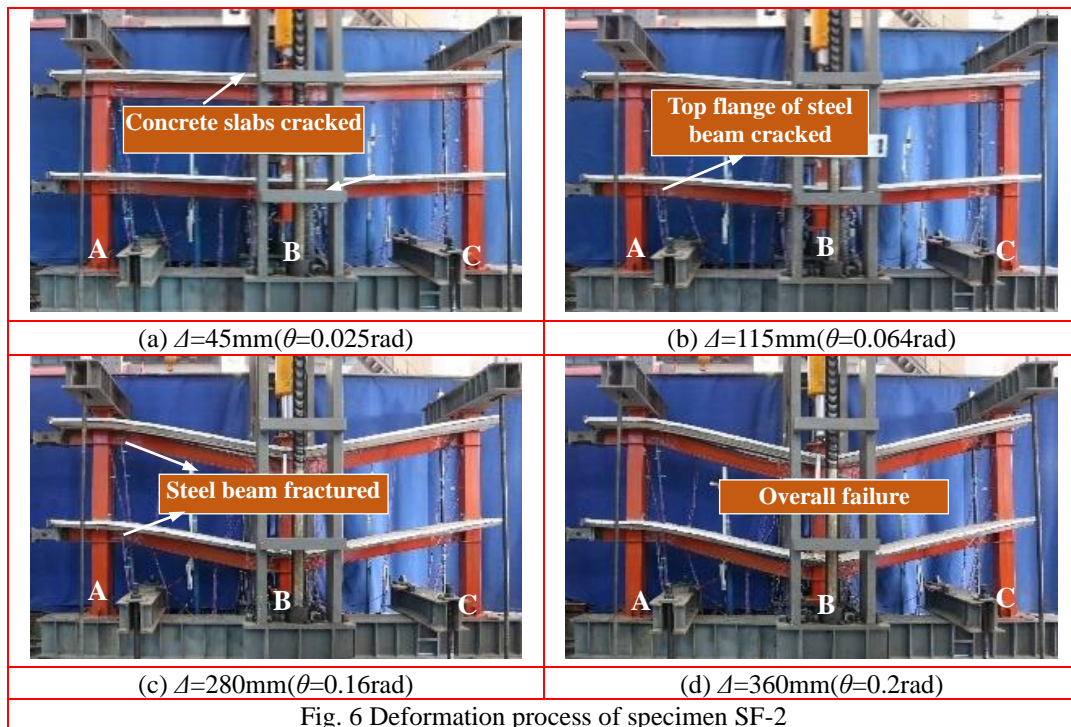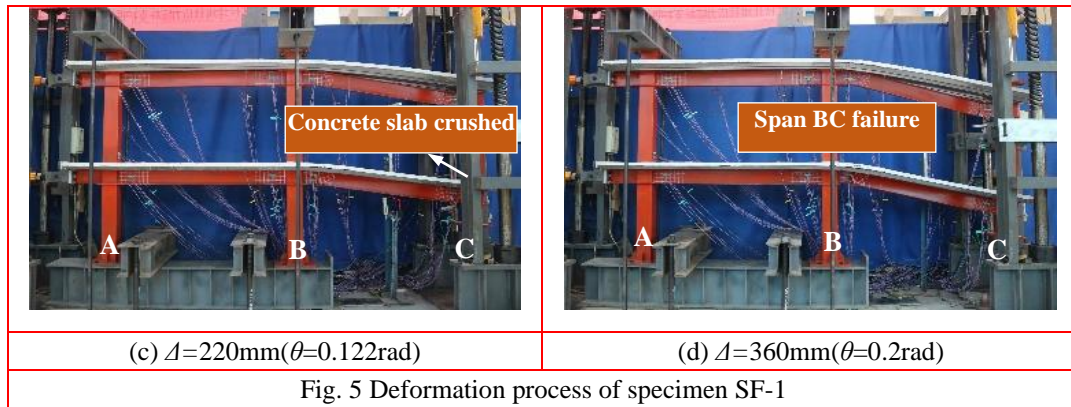
3.1.1 Overall failure characteristics

Fig. 5 shows the deformation of specimen SF-1 at various stages. When the vertical deformation reached 45 mm, tensile transverse cracks appeared at span BC. The top flange of the upper steel beam just to the right of column B fractured first. Span AB showed no obvious deformation, as shown in Fig. 5(a). When $\varDelta$=102 mm, more tensile cracks were observed in the upper right beams. Local buckling in the lower right beam was observed, as shown in Fig. 5(b). As the load increased, the lower concrete slab was crushed, and the profiled steel decking also exhibited significant flexural deformation, as shown in Fig. 5(c). When the vertical displacement $\varDelta$=360 mm, the right beams fractured, as shown in Fig. 5(d).

Fig. 6 shows the development of deformation for specimen SF-2. From $\varDelta$=0 to $\varDelta$=45mm (see Fig. 6(a)), horizontal and longitudinal cracks appeared in the lower and upper concrete slabs sequentially. Cracks in steel beam just to the right side of column A were observed, and then separation between the composite slab and the steel beam was observed (see Fig. 6(b)). At $\varDelta$=280mm (see Fig. 6(c)), different degrees of cracking and buckling deformation were observed in the beam-column joint region of the BC span. Cracking was initially observed in the steel beam on the right side of column A, while significant local buckling was noted on the upper flanges of the upper and lower steel beams on the left side of column B. At $\varDelta$=360 mm, the lower beams to the right of column A and column B fractured severely.

The difference in the overall failure modes was within expectation. The failure of specimen SF-1 mainly concentrated in the failure span BC, and the failure of steel beams and composite slabs were observed for span BC only. By comparison, for specimen SF-2, varying degrees of damage occurred in both the left and right composite beams.

| (a) $\varDelta$=45mm(θ=0.025rad) | (b) $\varDelta$=102mm(θ=0.056rad) |

(c) Δ=220mm(θ=0.122rad)

(d) Δ=360mm(θ=0.2rad)

Fig. 5 Deformation process of specimen SF-1

(a) Δ=45mm(θ=0.025rad)

(b) Δ=115mm(θ=0.064rad)

(c) Δ=280mm(θ=0.16rad)

(d) Δ=360mm(θ=0.2rad)

Fig. 6 Deformation process of specimen SF-2

3.1.2 Local failure modes of steel beams

Once critical column members failed, the connecting beams were critical in terms of redistributing load to adjacent members (Wang *et al*. 2020). The failure modes of the steel beams and the progressive collapse are correlated. Therefore, it is necessary to understand the failure modes of beams. The local failure modes of specimen SF-1 and SF-2 are shown in Figs. 7-8, respectively.

For specimen SF-1, failure was mainly in the span BC. When the vertical displacement reached 45 mm, the top flange of the upper beam connecting column B cracked (see Fig. 7(f)). At Δ=57 mm, local buckling occurred at the web and bottom flange of the lower beam (see Fig. 7(b)). At Δ=75 mm, the bottom flange of the upper beam cracked (see Fig. 7(h)). At Δ=330 mm, the bottom flange ring decking of the lower beam cracked subsequently (see Fig. 8(d)). Meanwhile, the local buckling deformation to the right side of lower column B is shown in Fig. 7(a). At Δ=360mm, the cracks at the beam-to -ring plate connection extended to the web (see Fig. 7(g)). The cracks at the top flange also extended to 102mm into the web (see Fig. 7(e)).
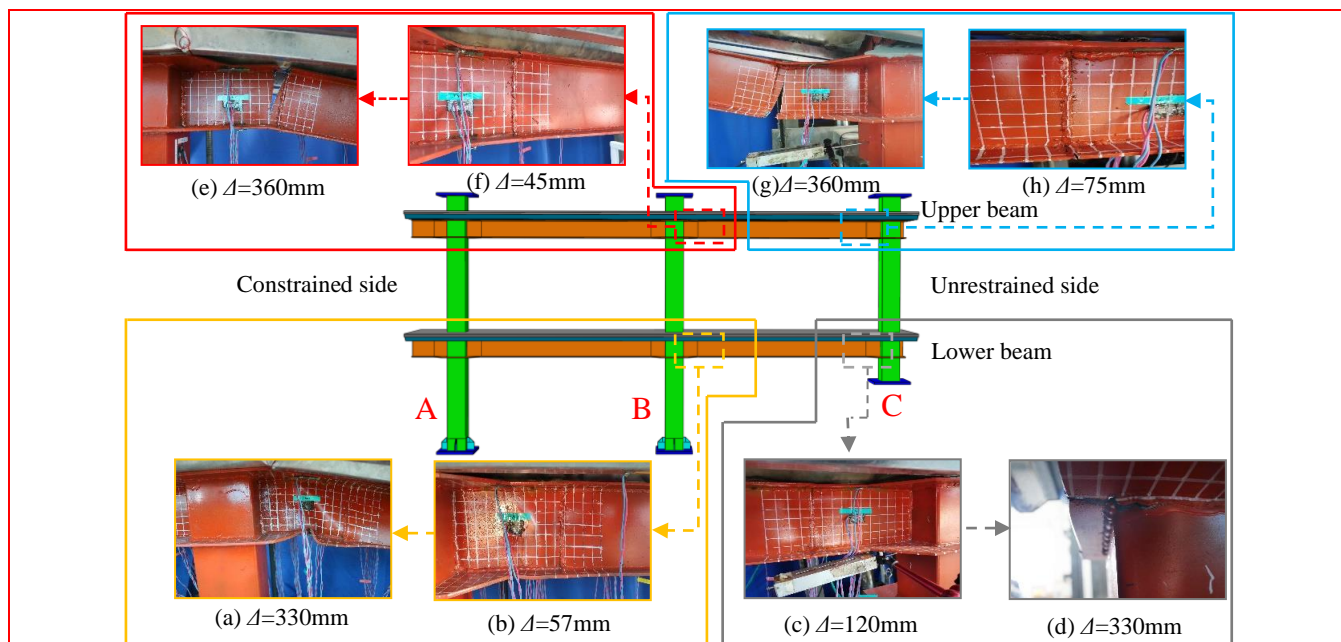
(e) *Δ*=360mm   (f) *Δ*=45mm   (g)*Δ*=360mm   (h) *Δ*=75mm

Upper beam

Constrained side   Unrestrained side

Lower beam

A   B   C

(a) *Δ*=330mm   (b) *Δ*=57mm   (c) *Δ*=120mm   (d) *Δ*=330mm

Fig. 7 Local failure modes of steel beams (SF-1)

(e) *Δ*=360mm   (f) *Δ*=360mm   (g) *Δ*=360mm   (h) *Δ*=360mm

Upper beam

Constrained side   Unrestrained side

Lower beam

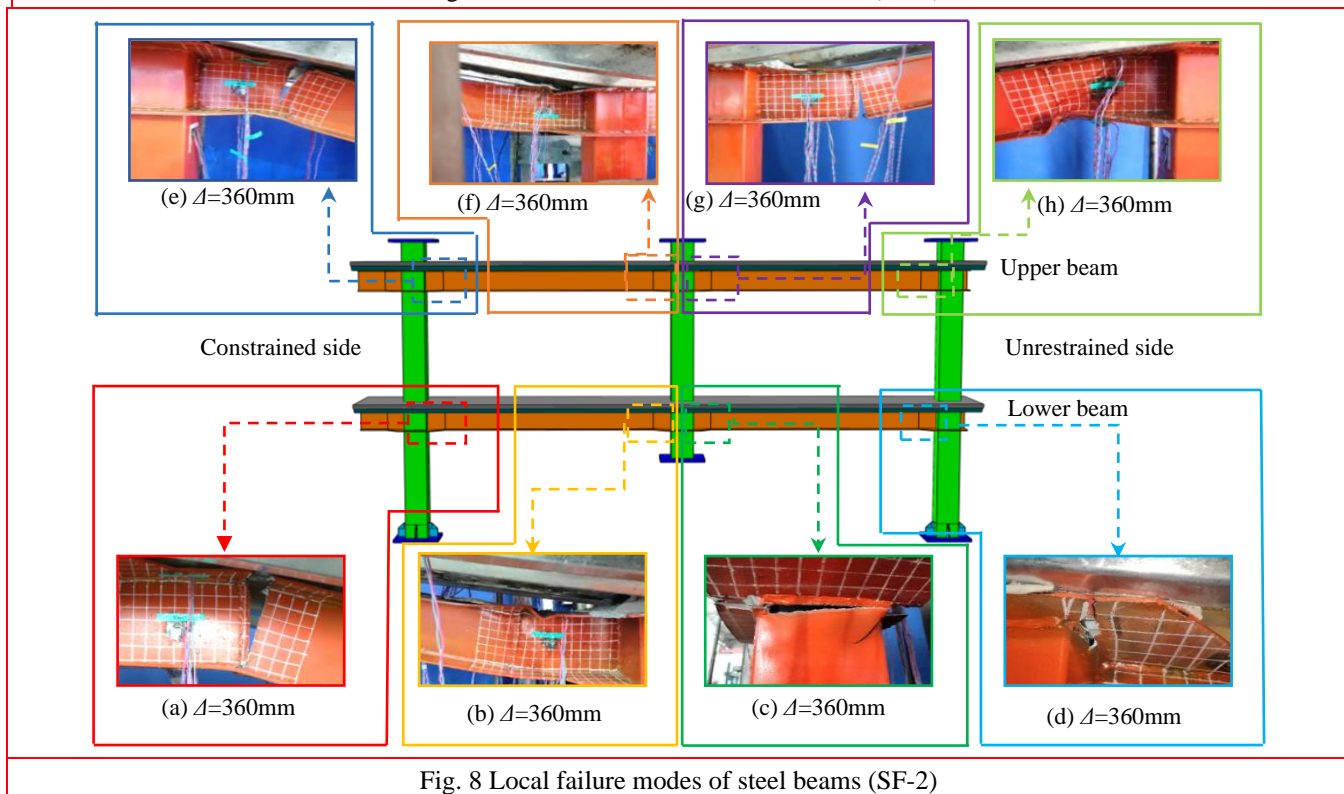(a) *Δ*=360mm   (b) *Δ*=360mm   (c) *Δ*=360mm   (d) *Δ*=360mm

Fig. 8 Local failure modes of steel beams (SF-2)

For specimen SF-2, the failure was dominated by fracture and buckling of the beams. The top flange of the lower right beam cracked first, and then the top flange of the upper right beam and the bottom flange of the right beam cracked subsequently. The final failure modes of steel beams are shown in Figs. 8(a, e and g). The top flange of the left beam in the first and second story and the bottom flange of the left beam in the second story exhibited different buckling deformation.

The comparison shows that the failure of specimen SF-1 was mainly concentrated in the span BC. Span AB exhibited no obvious deformation, and the failure of the upper beam was before that of the lower beam. In contrast, failure modes of specimen SF-2 were cracking and buckling deformation in the beams, and the fracture of the lower beams was before that of the upper beams. The beams on the restrained side were damaged to a greater extent than the unrestrained side, indicating that if a middle column fails suddenly but the remaining structure does not collapse, then the beams connected to the stronger side may experience greater damage.

3.1.3 Local failure modes of composite slabs

Fig. 9 shows the cracks on the upper face of the lower slabs. For specimen SF-1, major cracks appeared to the right side of column B. Span AB developed minor cracks, mostly at the initial loading stage. For specimen SF-2, the

lateral cracks of span AB at failure stage were greater than that of span BC, plausibly because the horizontal boundary constraint was applied from the left side. Local cracks near column C were observed.

(a) Specimen SF-1

— Left concrete crack   — Right concrete crack   ▨ Concrete crush failure
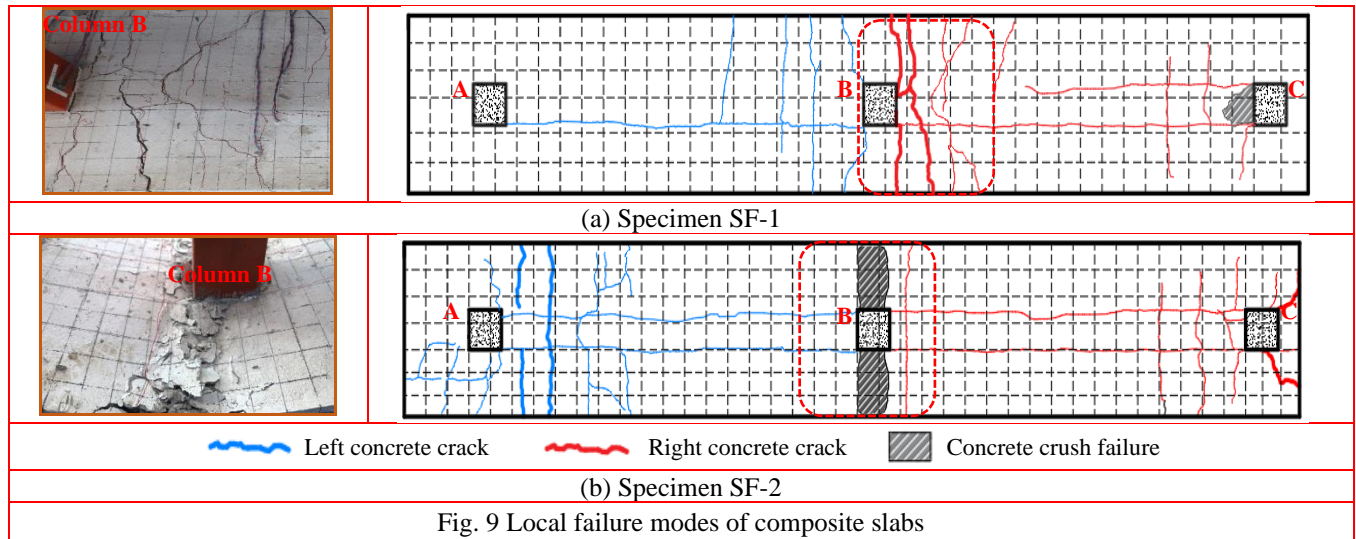
(b) Specimen SF-2

Fig. 9 Local failure modes of composite slabs

3.2 Vertical load-displacement curves

GSA (2013) and DoD (2016) recommend that collapse resistance of remaining structure may be used to evaluate the resistance to progressive collapse. Therefore, the resistance of the remaining structure is studied in this section. Fig. 10 shows the vertical load (P) versus vertical displacement (Δ) curves. Note P is the vertical collapse resistance, Δ is the vertical displacement of the failure column, and θ is the angle of the steel beam ($\theta=\Delta/L$, L is the column spacing). The $P-\Delta$ relationships can be divided into four stages, i.e., an elastic stage, an elastic-plastic stage, a stage of fracture development and a failure stage.
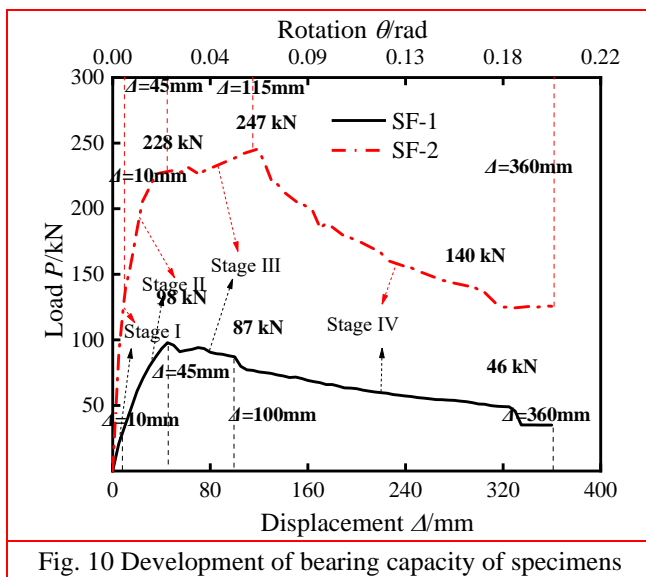

Fig. 10 Development of bearing capacity of specimens

At the initial loading stage, both specimens were in the elastic stage. The vertical load increased linearly with the vertical displacement. The maximum collapse resistance of specimen SF-1 was 98kN, and then began to drop slowly due to the failure of the top flange in the upper beam. However, due to the bending and the axial tension of composite beams, the collapse resistance of specimen SF-2 increased again when the vertical displacement reached 45mm. The maximum vertical collapse resistance value was 247kN, and then the collapse resistance began to drop slowly. For specimen SF-1 and SF-2, when the vertical displacement reached the collapse critical displacement value of 360 mm, as specified by GSA (2013), the collapse resistance of the remaining structure was 46kN and 140kN, respectively.
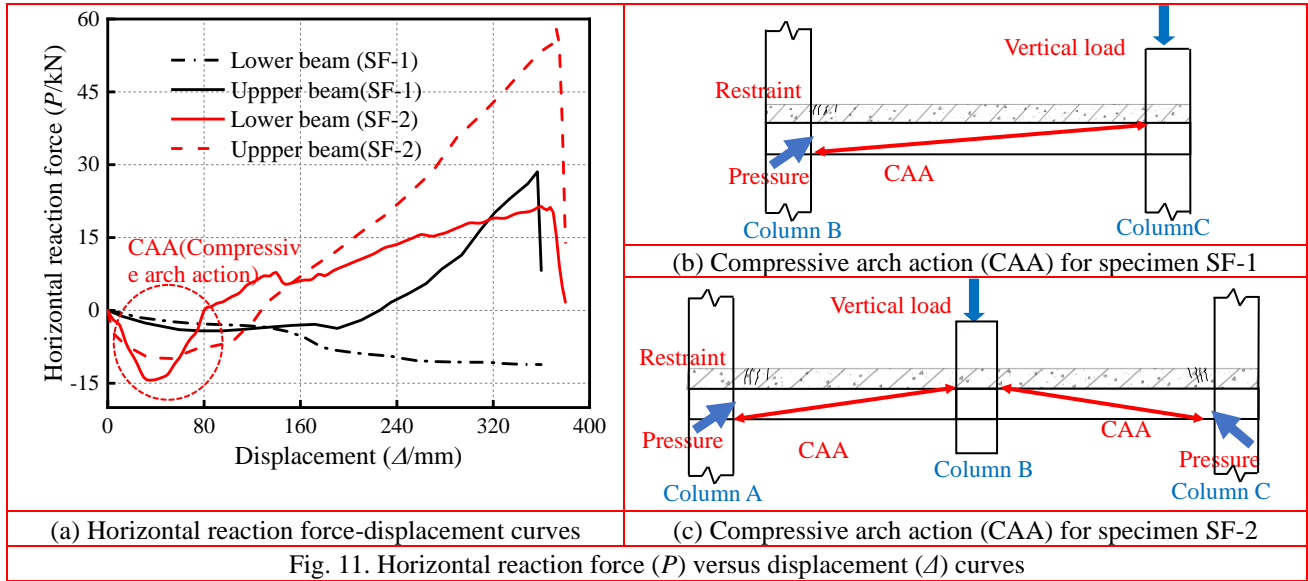
The difference in vertical collapse resistance was within expectation. The collapse resistance of specimen SF-2 was greater than two times the collapse resistance of SF-1. Because for specimen SF-1, the upper beam connected to the failure column did not form a tie force after the corner column was removed. Therefore, it was more likely for corner column failure scenario to develop local failure.

3.3 Horizontal reaction

The test facility (see Fig.3) featured a horizontal reaction frame at one end. The purpose was to simulate the situation where constraints exist at one side of the sub-frame. Two load cells mounted between the beam ends and the reaction frame were employed to monitor the horizontal reaction. Fig. 11 plots the measured horizontal reaction force (P) against the vertical displacement (Δ) curves. Compressive reaction force is negative and tensile reaction force is positive.

| (a) Horizontal reaction force-displacement curves | (b) Compressive arch action (CAA) for specimen SF-1 |
| | (c) Compressive arch action (CAA) for specimen SF-2 |

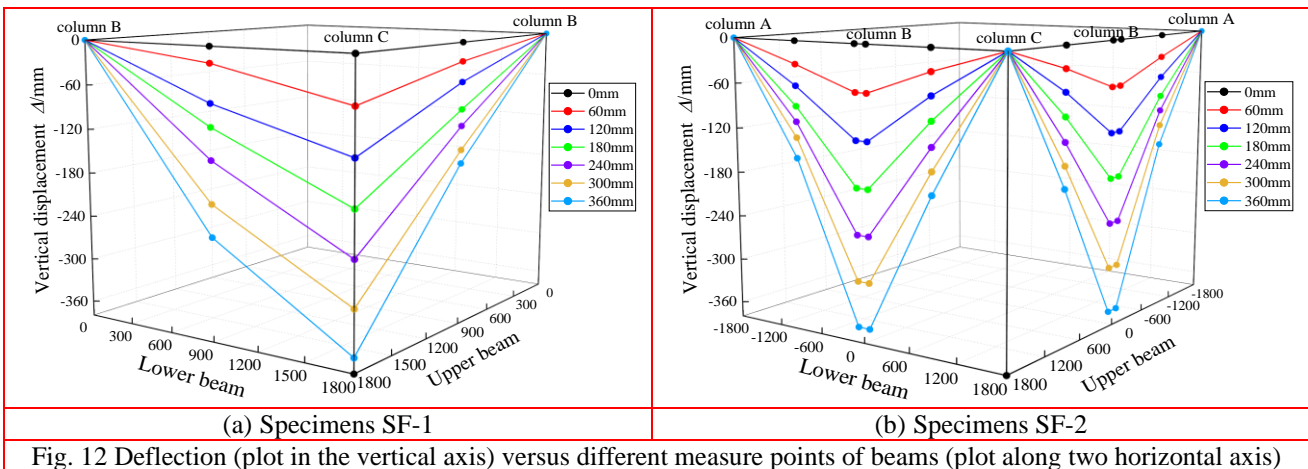Fig. 11. Horizontal reaction force (*P*) versus displacement (*Δ*) curves

In specimen SF-1, the horizontal reaction at the end of the lower beam remained compressive, attributed to compressive arch action (CAA) during the early stage. With the vertical displacement of the failed column increasing, the slight inward inclination of the failed column induces compression on the lower beam, leading to a subsequent rise in compressive stress. This tendency is evidenced by the final failure mode of specimen SF-1 depicted in Figs. 5(a-d). The horizontal reaction for the upper beam changed from compression to tension when the vertical displacement reached 226 mm. For specimen SF-2, the developments of the horizontal reaction in the lower and upper beams exhibited similar trends. The horizontal reaction of both the lower and upper beams was in compression at the early stage, then changed to tension as the vertical displacement increased. The compression at the early stage was plausible due to the arch action formed within the frame.

When the vertical displacement exceeded 160 mm, the horizontal reaction of the upper beams was greater than those of the lower beams. This suggests that the upper beams had a greater contribution to the resistance over this stage. The horizontal reaction of specimen SF-2 was greater than that of SF-1. It appears that the horizontal tie force of the adjacent beams can effectively strengthen the vertical collapse resistance of the specimens.

3.4 Vertical displacement of specimens

To observe the development of beam deflection over time, displacements are plotted against locations along the beams in Fig.12. For the convenience of comparison, the lower beam and upper beam are plotted in the left and right planes, respectively, and the vertical displacement relationships are to complement the failure modes in Figs. 5-6. For specimen SF-1, more deformation could be observed for the lower beam, particularly when the vertical displacement exceeded 240 mm. This is mainly due to the local buckling at the beam (see Fig.7a). For specimen SF-2, both beams followed a similar development. The difference in displacement between the two beams was negligible, confirming the symmetrical deformation in Fig. 6.

| (a) Specimens SF-1 | (b) Specimens SF-2 |

Fig. 12 Deflection (plot in the vertical axis) versus different measure points of beams (plot along two horizontal axis)

3.5 Distribution of strain along the depth of beams

This subsection presents the measured strain. To

illustrate the strain variation against beam depth in the elastic stage, discrete strain values corresponding to different load values are plotted in Figs. 13-14, respectively. Compressive strain was taken as the negative, and tensile strain was positive.

For specimen SF-1, span AB showed no obvious deformation (see Fig.5). Therefore, the strain of cross-sections B1 to B4 in span BC is plotted. For cross-sections B1 and B2, the bottom flange of specimen SF-1 was under tension and the top flange was compression. At the end of

the elastic stage, the vertical load reached 90kN. Consequently, the tension zone enlarged. The neutral axis of the beam moved downward, as shown in Figs. 13(a)-(b). For specimen SF-1, the entire cross-section B3 was in compression. The steel beams exhibited local buckling, as shown in Fig. 7(a). For B4, the top flange was in tension, and the bottom flange was compression. According to Fig. 7(f), the failure of the steel beam was initiated by the cracking from the top flange and subsequent propagation into the web.
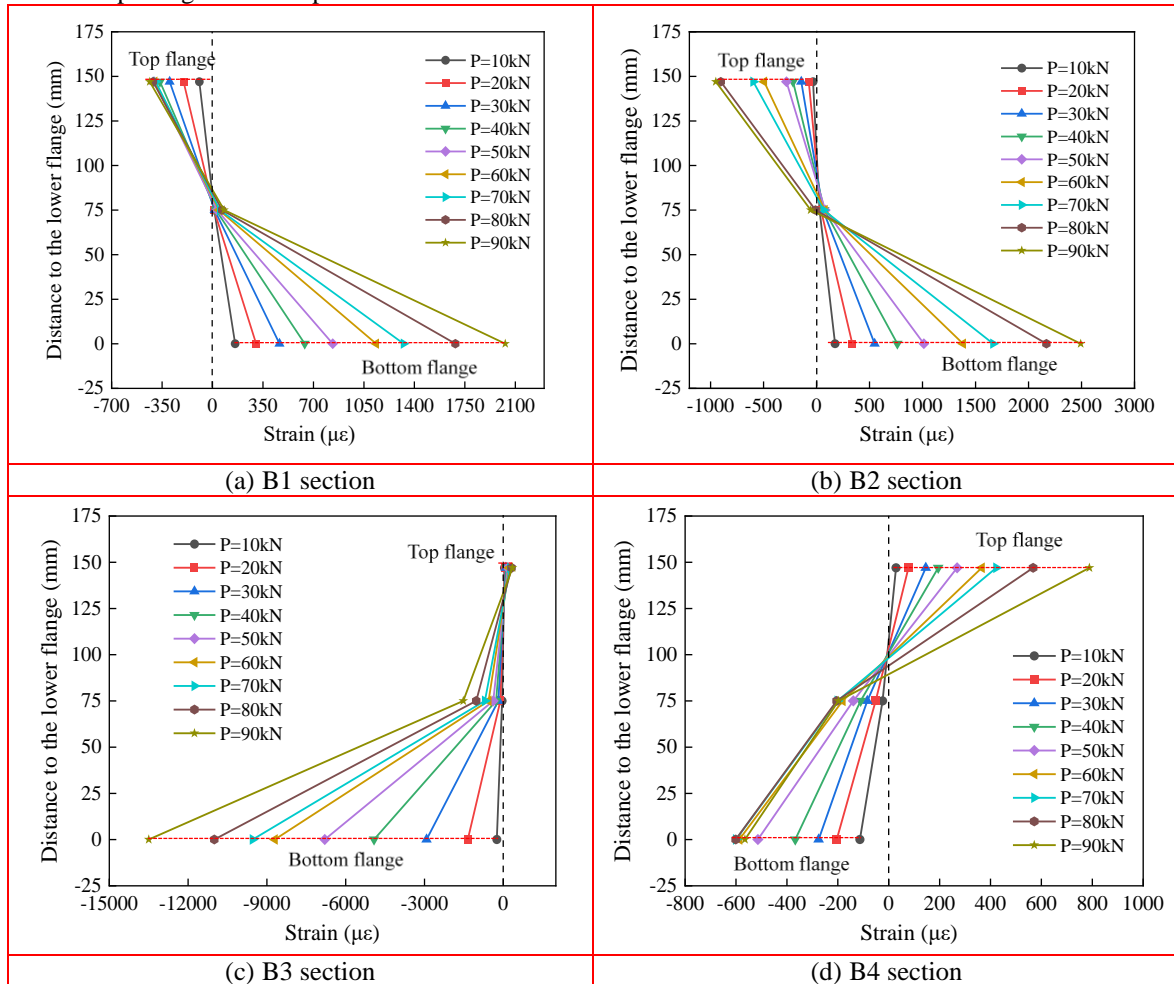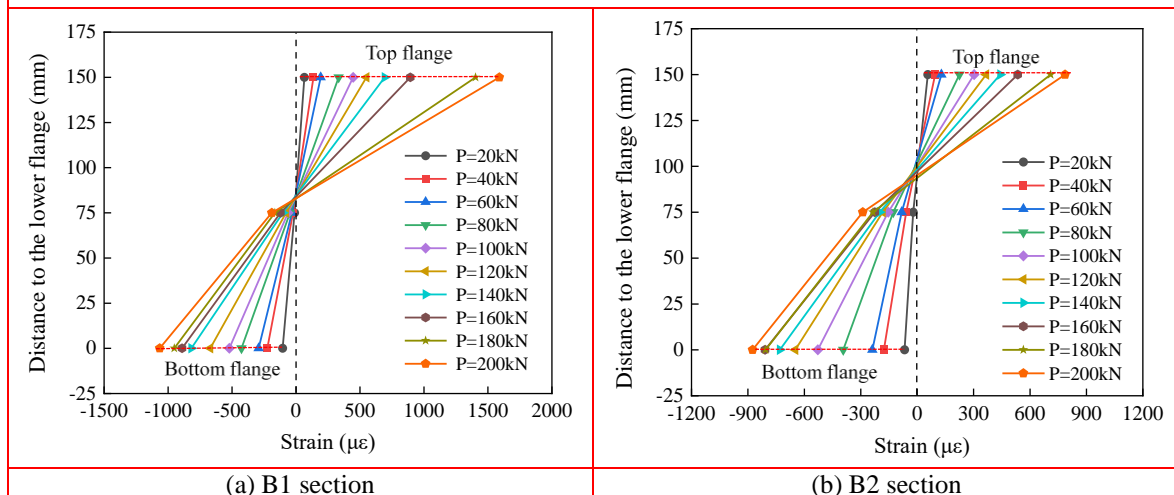

(a) B1 section

(b) B2 section

(c) B3 section

(d) B4 section

Fig. 13 Distribution of strain along the depth of beams at various load levels (SF-1)

(a) B1 section
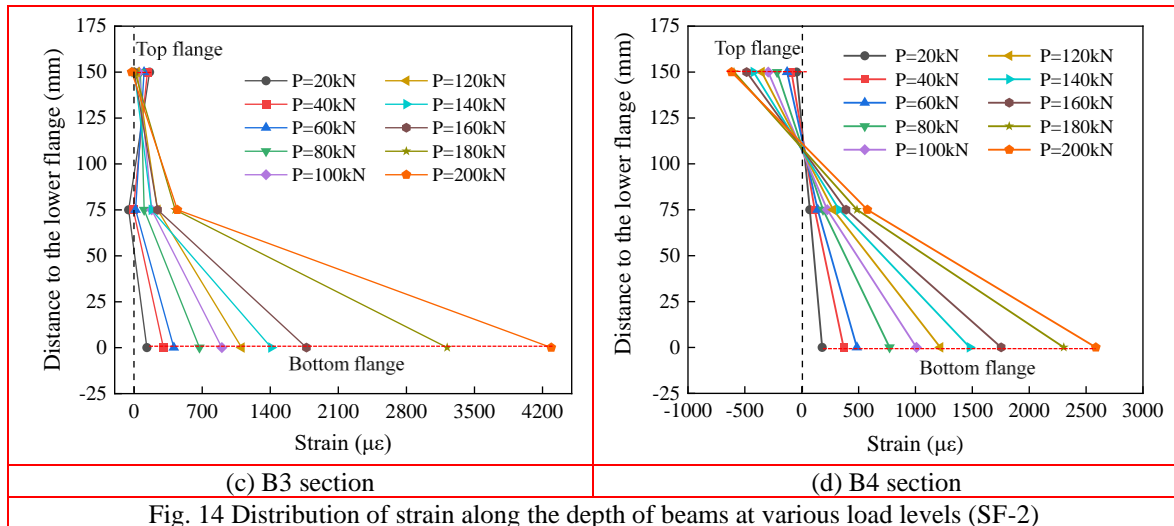
(b) B2 section

| (c) B3 section | (d) B4 section |

Fig. 14 Distribution of strain along the depth of beams at various load levels (SF-2)

For specimen SF-2, the strain development along beam depth was opposite to that of specimen SF-1, as shown in Figs. 14(a)-(b). The neutral axis shifted to the bottom flange, as shown in Figs. 14(c)-(d). The comparison of the strain distribution at cross-sections B1 and B3, B2 and B4 suggests that the strain near the failure column was greater. This can be confirmed by the local failure modes in Figs. 8(c)-(d) and (g)-(h).

4 Numerical analysis

To complement the experimental results and to further investigate the mechanical behavior of the frames, a refined finite element (FE) model was established using ABAQUS/Implicit. The FE modelling was first validated against the test data and then utilized to study the effect of factors that cannot be studied in tests.

4.1 Numerical model

4.1.1 Modelling method

Fig. 15 shows the FE model for specimen SF-2. Truss elements (T3D2) were used to simulate the longitudinal and transverse reinforcements. The profiled steel decking, steel tube and steel beam were modeled using shell elements (S4R). 8-node linear reduced integration solid elements (C3D8R) were utilized for concrete, shear studs, and other components. Surface to surface contact was adopted for the steel tube to core concrete interface, and the profiled steel decking to slab concrete interface. The tangential friction coefficient was defined as 0.25, and hard contact was used for the normal behavior. The shear studs and reinforcement were embedded in the concrete slab. 'Tie' constraint was used to simulate the welds between steel components. The mesh sizes were approximately 60 mm for the concrete and profiled steel decking, and approximately 40 mm for steel beams and columns. In the joint area, the mesh size was reduced to 20mm. Load was applied by displacement control.
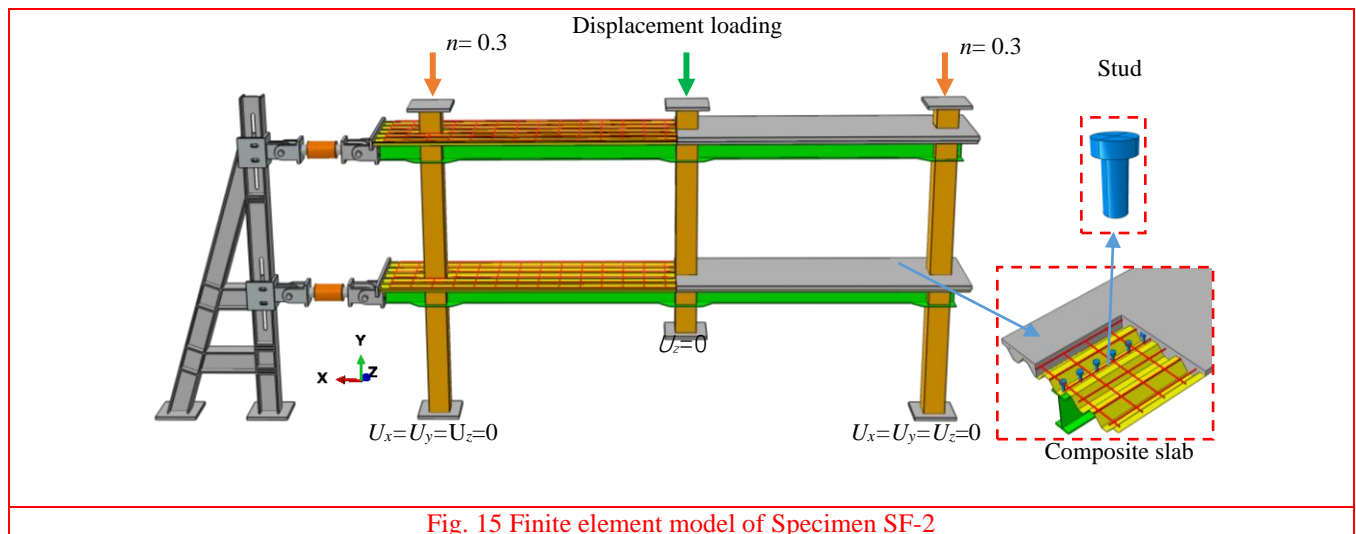

Fig. 15 Finite element model of Specimen SF-2

4.1.2 Material models

Steel

To consider the ductile fracture of steel and to improved convergence in simulation, the non-coupling

ductile fracture model (Gruben *et al*. 2011) was used to distinguish the constitutive and fracture properties. The constitutive models were proposed by Esmaeily and Xiao (2005). Strain is used as an indicator to determine whether fracture has occurred. The constitutive behavior and fracture behavior in this model are independent of each other.

The stress-strain relationship was defined for the elastic stage, yield plateau and strain hardening. The stress-strain curves are controlled by factors k_1, k_2 and, k_3, as given by Eq. (1).

$$\sigma = \begin{cases} E_s \varepsilon & (\varepsilon \le \varepsilon_y) \\ f_y & (\varepsilon_y < \varepsilon \le k_1 \varepsilon_y) \\ k_3 f_y + \dfrac{E_s(1-k_3)}{\varepsilon_y(k_2-k_1)^2}(\varepsilon - k_2 \varepsilon_y)^2 & (\varepsilon > k_1 \varepsilon_y) \end{cases} \quad (1)$$

The stress-strain relationship of steel is shown in Fig. 16. When the stress reaches the equivalent plastic strain ($\overline{\varepsilon}_0^{pl}$), steel begins to enter the evolution mode of plastic damage (Wang *et al*. 2020). As shown by the red curve in Fig. 16, the descent section of the curve is the damage evolution at the strain, which is between the equivalent plastic strain ($\overline{\varepsilon}_0^{pl}$) and the fracture strain ($\overline{\varepsilon}_f^{pl}$). The damage evolution path of steel can be controlled using the damage factor *D*. When *D* = 0, steel is not seen as damaged. When *D*=1, steel is deemed completely failed. *D* is a function of the equivalent plastic strain of steel, as shown in Eq. (2).

$$D = 1.3 \left(\frac{\overline{u}^{pl}}{\overline{u}_f} \right)^{7.6} \quad (2)$$

Where $\overline{u}^{pl}$ is the plastic displacement of steel, and $\overline{u}_f$ is the ultimate displacement of steel during tensile fracture.
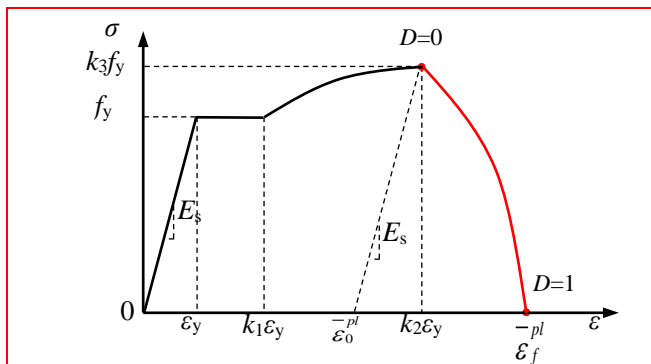

Fig. 16 Stress-strain curve of steel

Concrete

The concrete damaged plasticity model was used to simulate the behavior of the concrete in compression and tension. The confined concrete model proposed by Han

(2016) was used. This model considers the constraint effect of the steel section. For the concrete in slabs, the stress-strain relationship given in Chinese code GB50010-2010 was adopted.

4.2 Validation of FE model

Fig. 17 compares the predicted load-displacement curves with experimentally measured ones. It shows that the predicted curves are slightly higher than the test results, particularly for the post-peak stages. This is plausibly due to imperfections, such as welds between the steel ring plates and CFST columns. In terms of the maximum collapse resistance, the predicted values are reasonably close to the measured ones. For specimen SF-1 and SF-2, the differences between the predicted and measured collapse resistance are 6.2% and 3%, respectively.

Fig. 18 compares predicted failure modes with test observation. The FE models reproduce the failure process, such as local bucking (see Figs.8 (a)-(d)) and cracking of steel beam (see Figs.8 (b)-(c)). The predictability of the FE model is deemed acceptable. Therefore, the FE models will be used to further study the frame behavior and to conduct a parametric study.

The tensile damage of concrete slabs of specimen SF-1 and specimen SF-2 is shown in Fig. 19. The tensile damage of the concrete slabs is consistent with the test results in Fig. 9. For specimen SF-1, tensile damage mainly occurred in span BC. Transverse tensile cracks appeared on the left and right sides of column B. Local concrete crushing occurred in concrete slab near column A, as shown in Fig. 19(a). For specimen SF-2, tensile damage appears more severe near columns A and C. In the large deformation stage, compressive damage is more localized to areas close to column B, as shown in Fig. 19(b).
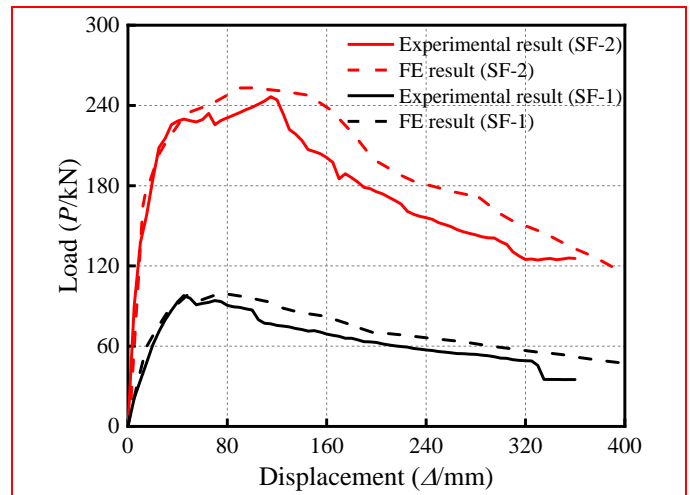

Fig. 17 Comparison of load-displacement curves obtained from experiment and simulation

Stress spectrum	(a) Right side of column B on the lower beam in SF-1	(b)Right side of column B on the upper beam in SF-1	(c)Right side of column B on the upper beam in SF-2	(d) Left side of column C on the upper beam in SF-2
S, Mises (Avg:75%) 391 359 326 293 261 228 196 163 130 98 65 33 0				

Fig. 18 Comparison of local failure modes between test and FE models

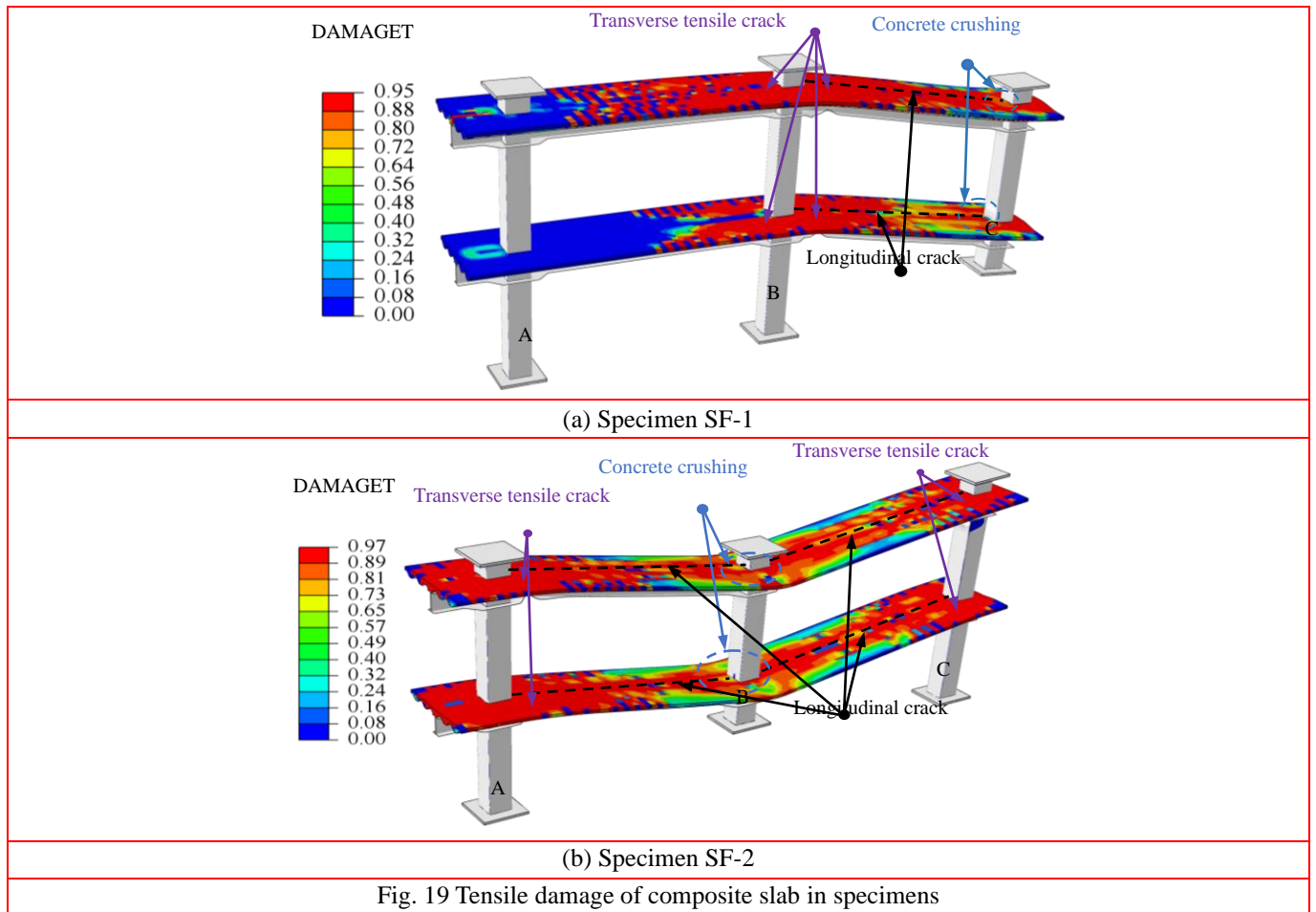(a) Specimen SF-1

(b) Specimen SF-2

Fig. 19 Tensile damage of composite slab in specimens

4.3 Analysis of resistance mechanism

According to the local failure modes of steel beams, the fracture of steel beam appears to be a critical cross-section for the remaining structure. Therefore, it is of interest to further study the stress development of such a section. This subsection takes cross-section B4 as an example. The stress vectors depicted in Fig. 20 correspond to the x-direction in the finite element analysis results.

For specimen SF-1, in the elastic stage (see Fig. 20(a)), stress distribution exhibits a linear pattern, with the top flange in tension, and the bottom flange in compression. As the vertical displacement increased, the tensile stress of the top flange increased. Consequently, the neutral axis moved downwards. The top of the cross-section finally fractured, reflected by the decrease and the disappearance of the stress vectors of the top flange and web. For specimen SF-2 [see Fig. 20(b)), by contrast, cross-section B4 in the elastic stage presented a stress distribution opposite to the specimen SF-1. The top flange was in compression, and the bottom flange was in tension. As the vertical loading increased, the tension zone increased until a fracture at the bottom of the steel beam appeared. Finally, the stress of the lower half of the cross-section was nearly 0.

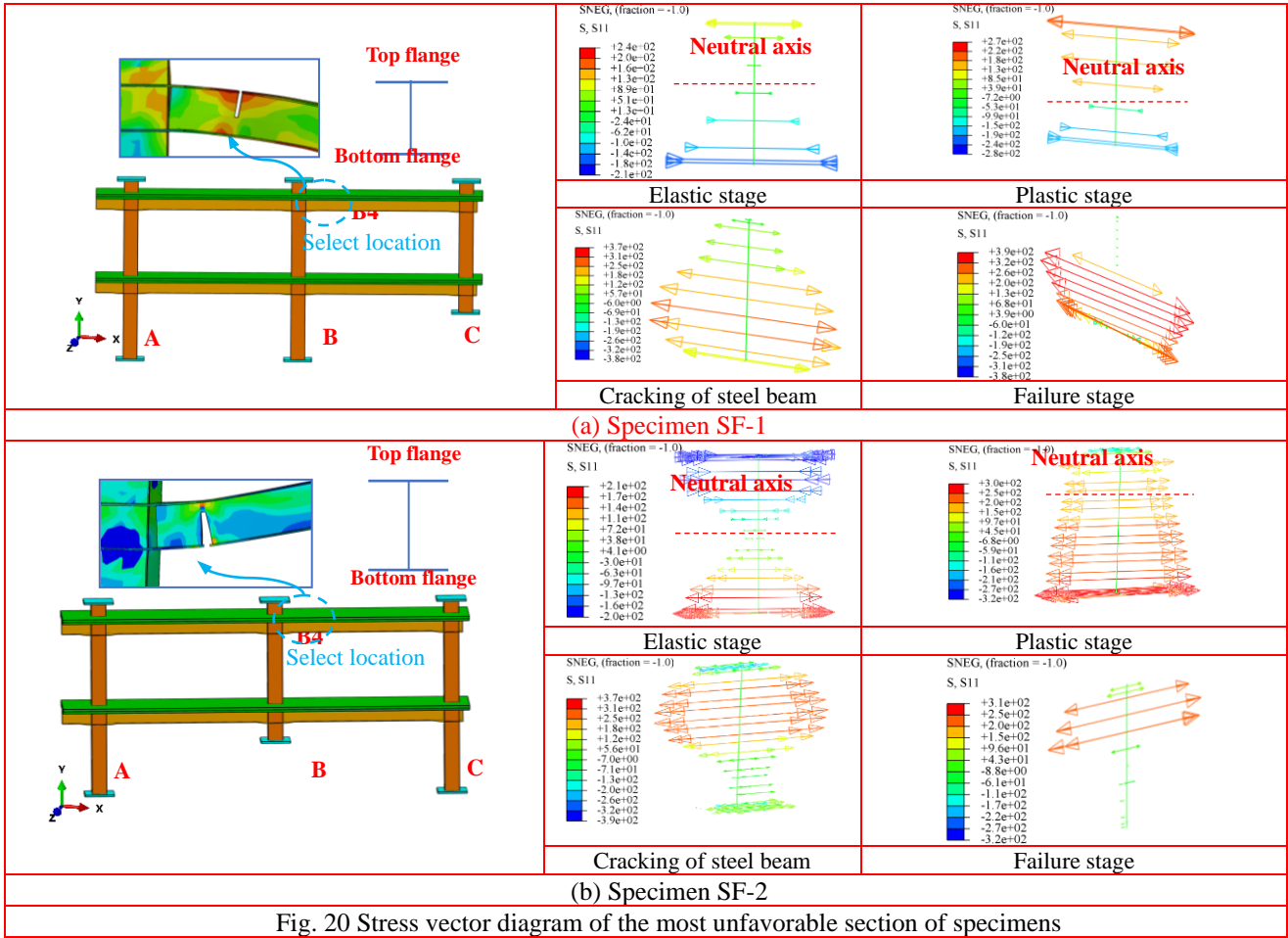(a) Specimen SF-1

(b) Specimen SF-2

Fig. 20 Stress vector diagram of the most unfavorable section of specimens

To further study the mechanism of load transfer, the axial force (left-hand axis) against vertical displacement (bottom axis) and bending moment (right-hand axis) against beam rotation (top axis) curves are plotted in Fig. 21. M and P are the bending moment and axial force of the beams, and M_{max} and P_{max} are the maximum bending moment and maximum axial force.

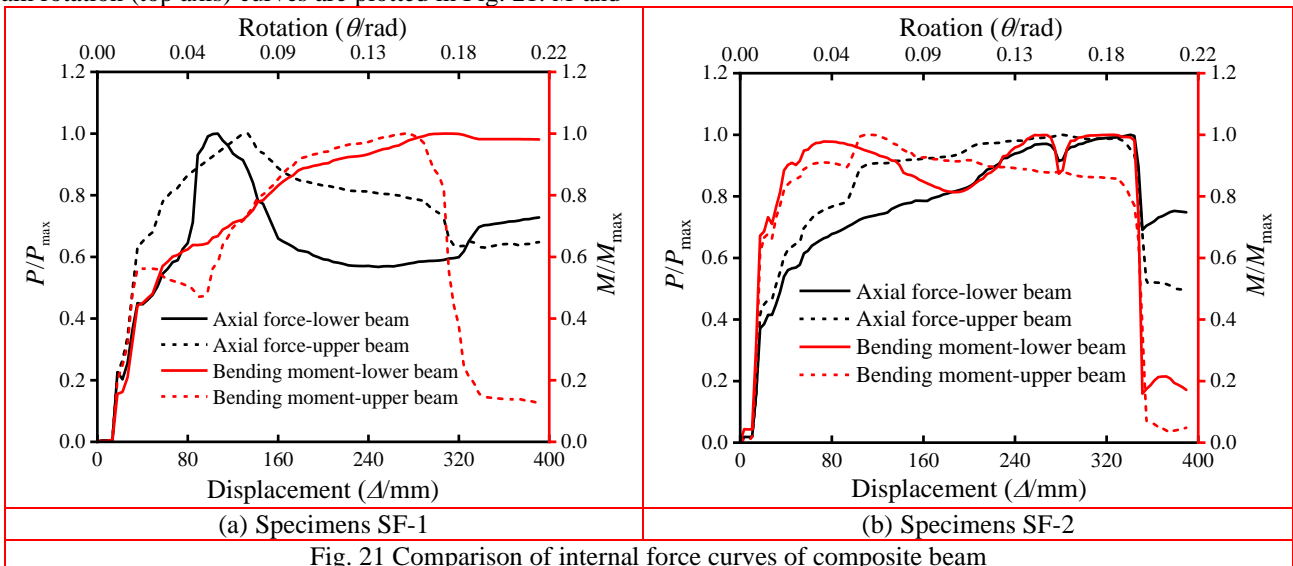(a) Specimens SF-1

(b) Specimens SF-2

Fig. 21 Comparison of internal force curves of composite beam

It is found that: (1) For specimen SF-1, the axial force of the lower beam is mostly less than that of the upper beam, indicating that the upper beam significantly contributed to the main collapse resistance. When the vertical displacement reached 280 mm, the upper beam of span BC fractured, resulting in a sharp decline in bending moment curve. (2) For specimen SF-2, the axial force and the bending moment of the lower beam are slightly less than those of the upper beam. The premature cracking of the shear studs led to the fracture of the upper beam. The bending moment and axial force of the upper beams significantly decrease in the large deformation. (3) For the middle column removal scenario (specimen SF-2), both flexural mechanism and catenary mechanism contributed to

the resistance to progressive collapse. By comparison, for the corner column removal scenario (specimen SF-1), it was the flexural mechanism that mainly contributed to the collapse resistance, especially in the large deformation stage.

4.4 Contribution of composite slabs

As a main bearing component of structure, slab had an important effect on progressive collapse resistance of building structures (Pham *et al.* 2017). Composite slabs with profiled decking and RC slabs are widely adopted in practice. Therefore, three cases were considered and analyzed in this subsection. They are: (1) frame with composite slabs, (2) frame with RC slabs, and (3) frame without slabs.

4.4.1 Load-displacement curves

Fig. 22 compares the vertical load (P) versus vertical displacement (Δ) curves. Clearly, the P-Δ curves for the cases without slab are lower than those with slabs. For the corner column removal scenario, the collapse resistances of the frame without slabs and with RC slabs are 35% and 17% lower than that of the case with composite slabs. For the middle column removal scenario, the corresponding reductions are 51% and 38%. This confirms that composite slabs contribute to collapse resistance significantly.
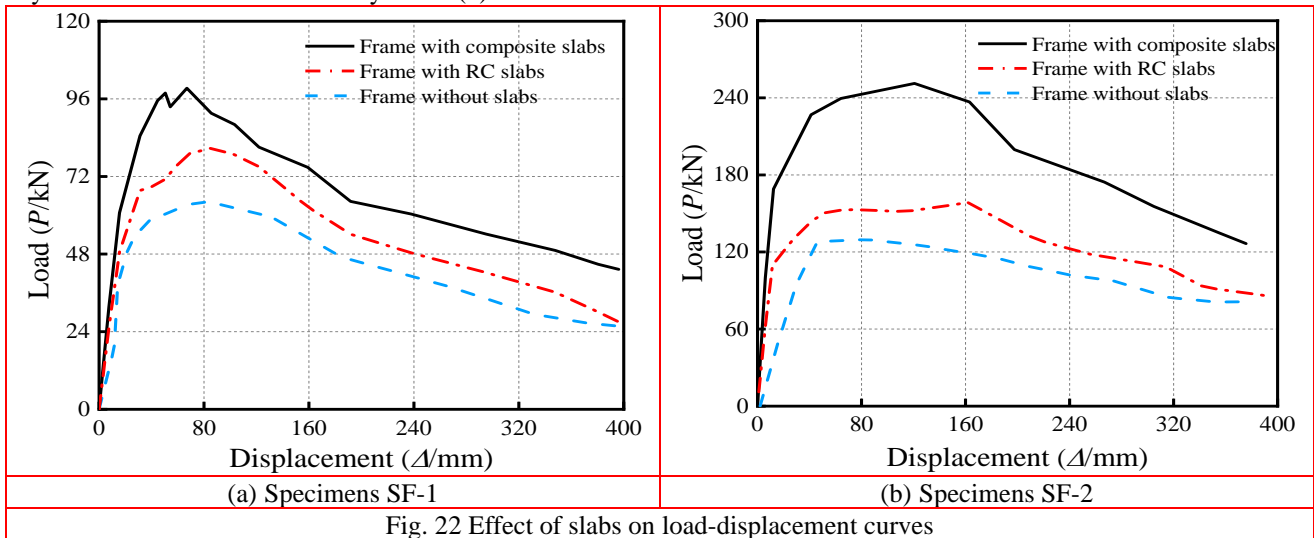

(a) Specimens SF-1	(b) Specimens SF-2

Fig. 22 Effect of slabs on load-displacement curves

4.4.2 Resistance contribution of composite slab

Fig. 23 illustrates the contribution of the steel beam to collapse resistance, with the contribution of steel beams represented below the curve and that of composite floor slabs depicted above the curve. For specimen SF-1, the beam accounts over a half of the resistance in the early stage. Despite some fluctuation, the contribution of the beam increased until the local buckling and fracture occurred (see Figs. 7(b)-(h)). For specimen SF-2, the composite slab carries over 80% of the collapse resistance in the beginning. Then it sees a drop as the displacement increases to about 50 mm. Afterwards, the resistance contribution of composite slabs increases gradually. When the vertical displacement reaches 241 mm, the contribution of beam gradually increases. This suggests that the axial tension that develops in beam in the late stage provides resistance. By comparison, the collapse resistance of SF-1 is provided by the steel beam and composite slab sequentially.
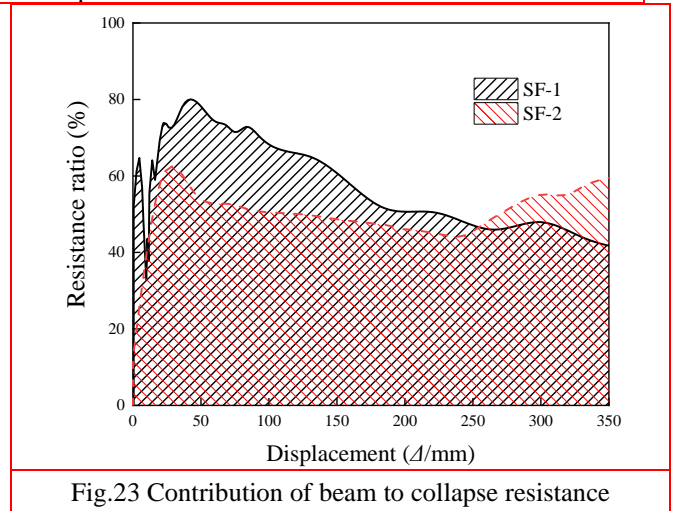

Fig.23 Contribution of beam to collapse resistance

4.5 Influence of horizontal boundary constraints

According to Section 3.3, the horizontal axial constraints had a significant effect on the collapse resistance of the remaining structure. Therefore, it may be of interest to study the effect of horizontal boundary conditions on collapse resistance. Three sets of additional boundary conditions are considered, i.e., without horizontal constraints, symmetrical and unsymmetrical boundary constraints. Note that symmetrical constraints were applied to the case of middle column removal only. Fig. 24 shows

the three boundary conditions for specimen SF-2.

Fig. 25 compares the load P-Δ curves for different boundary conditions. For specimen SF-1 (see Fig. 25(a)), the introduction of horizontal constraints on one side only has a limited effect on P-Δ curves. For specimen SF-2 (see Fig. 25(b)), the horizontal constraint has a more significant effect on P-Δ curves. When the asymmetric constraint is removed, the collapse resistance decreases by 34.8%. When symmetrical constraints are adopted, the collapse resistance increases by 1.8 times. This is plausibly because symmetrical constraints allow the frame to develop an increasing axial force in the beam.

(a) No boundary constraints

(b) Unsymmetrical boundary constraint
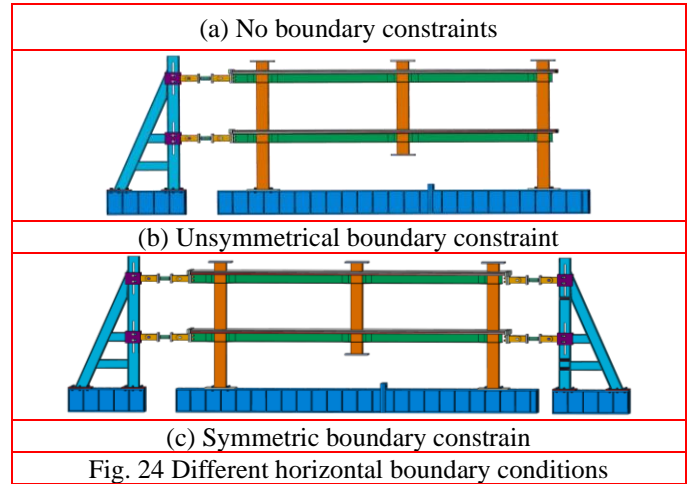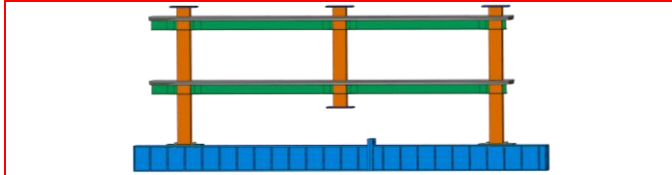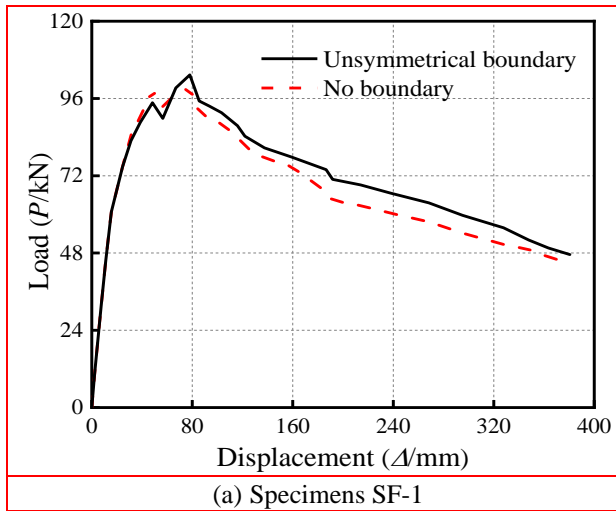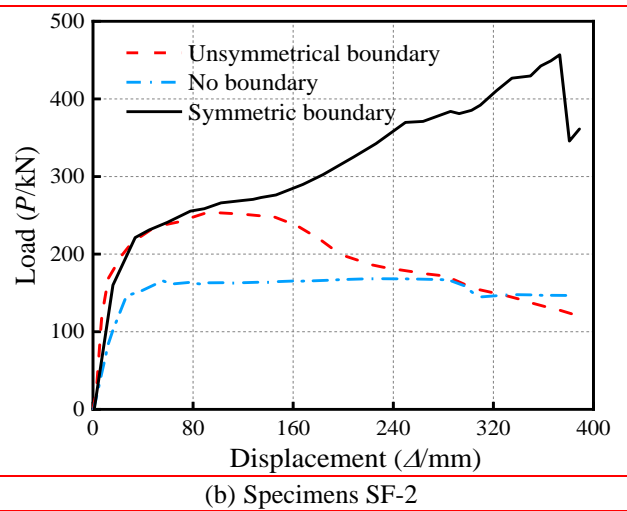

(c) Symmetric boundary constrain

Fig. 24 Different horizontal boundary conditions

(a) Specimens SF-1

(b) Specimens SF-2

Fig. 25 Comparison of load-displacement curves

4.6 Influence of column load ratio

This subsection studies the effect of load ratio of the non-failure columns. Three cases are studied, i.e., a case where no load is applied, and two cases with load ratios of 0.3 and 0.6, respectively. The load ratio is defined as $n=N_0/N_u$, where N_0 is the applied axial load, N_u is the buckling resistance.

Fig. 26 shows the effect of load ratio on load-displacement curves. For Specimen SF-1, load ratio appears to show a limited effect on the collapse resistance. By contrast, load ratio has a greater effect on the middle column removal scenario. For both scenarios, the collapse resistance of the remaining structure tends to increase as load ratio increases. This is plausibly because load applied to adjacent non-failure columns acted as a restraint to the failure column.
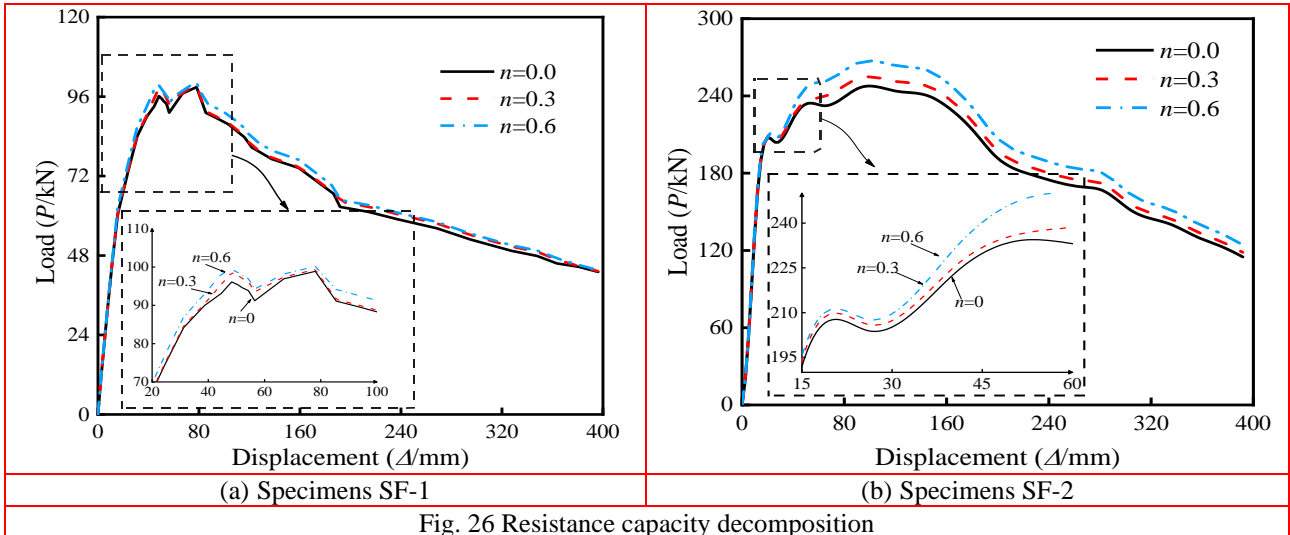
(a) Specimens SF-1	(b) Specimens SF-2
Fig. 26 Resistance capacity decomposition	

5 Simplified calculation of collapse resistance

To deepen understanding of the specimen's internal forces during loading and to adequately predict test results, this section introduces a simplified calculation method grounded in elastic theory. This method aims to evaluate the collapse resistance of the remaining structure under various column removal conditions. Given the fracture of the steel beams and the large deformation of the frames at the late stage, predicting the post-peak behavior appears challenging. Therefore, the simplified calculation in this section focuses on the pre-peak stage. It is assumed that elastic theory may be applied for this pre-peak behavior. The measured elastic strain data are, therefore, used to calculate the internal forces of composite beams. The axial force and bending moment of the composite beam are calculated by the axial strain of the steel beam, reinforcement, and profiled steel decking from a same cross-section. Fig. 27 shows the simplified calculation diagrams for the collapse resistance for the corner/middle column removal scenario.

(a) Corner column removal scenario (SF-1)

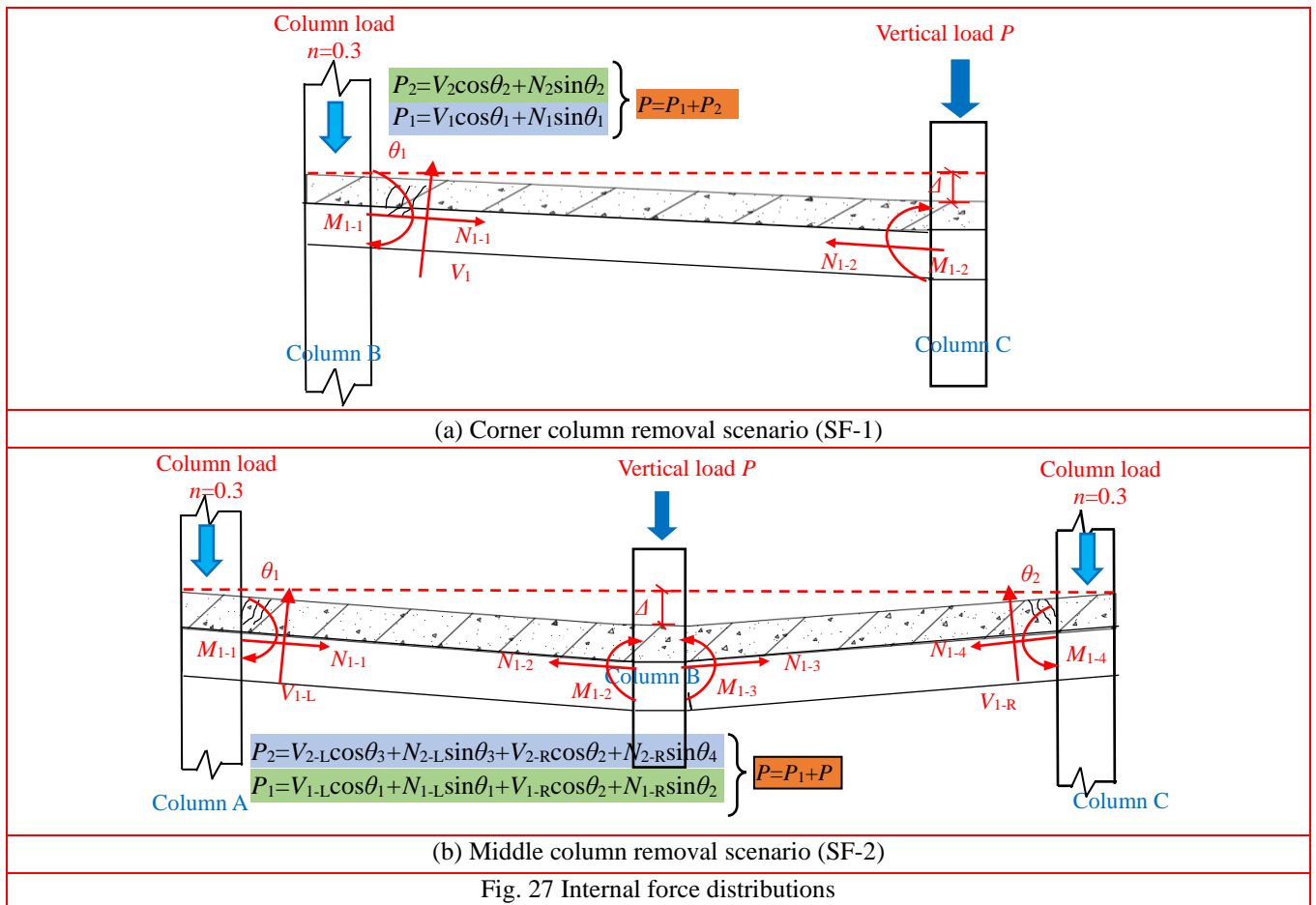(b) Middle column removal scenario (SF-2)

Fig. 27 Internal force distributions

According to the experiment and numerical analysis, the vertical collapse resistance of the frame is composed of the bending moment and the axial tension of the composite beam. In the two specimens, the bending moment M1-1 and axial force N1-1 at the beam end can be calculated from Eqs. (3)-(4), respectively. The axial force N_1 and shear force V_1 of the composite beam in the first story can be calculated according to the bending moment and axial force of the beam end, as shown in Eqs. (5)-(6).

$$M_{1\text{-}1} = \frac{1}{2} W_Z E (\varepsilon_5 + \varepsilon_6 - \varepsilon_1 - \varepsilon_2) \tag{3}$$

$$N_{1\text{-}1} = \frac{1}{6} E_{S1} A_{S1} \sum_{i=1}^{6} \varepsilon_i + \frac{1}{4} E_{S2} A_{S2} \sum_{i=1}^{4} \varepsilon_i + \frac{1}{2} E_{S3} A_{S3} \sum_{i=1}^{2} \varepsilon_i \tag{4}$$

$$N_1 = \frac{1}{2} \left(N_{1\text{-}1} + N_{1\text{-}2} \right) \tag{5}$$

$$V_1 = \frac{M_{1\text{-}1} - M_{1\text{-}2}}{\sqrt{L^2 + \Delta^2}} \tag{6}$$

where W_Z is the section modulus of the composite beam. ε_5 and ε_6 are the measured strains at the bottom flange of the steel beam, and ε_1 and ε_2 are those at the top flange. The arrangement of the measuring points is shown in Fig. 4. E_{S1}, E_{S2} and E_{S3} are the elastic moduli of steel beam, reinforcement and profiled steel decking, A_{S1}, A_{S2}, A_{S3} are the cross-sectional area, L is the initial spacing of composite beam, Δ is the vertical displacement of the failure column (column C in SF-1 and column B in SF-2).

For specimen SF-1, the vertical collapse resistance P, taken as the sum of the vertical components of shear force and axial force of composite beams, as shown in Fig. 27(a), can be determined by Eqs. (7)-(9). The vertical resistance of specimen SF-2 adopts a similar calculation method, as shown in Fig. 27(b).

$$P_1 = V_1 \cos\theta_1 + N_1 \sin\theta_1 \tag{7}$$

$$P_2 = V_2 \cos\theta_2 + N_2 \sin\theta_2 \tag{8}$$

$$P_{SF\text{-}1} = P_1 + P_2 \tag{9}$$

where P_1 and P_2 are the vertical resistance provided by the composite beams, respectively, V_1 and V_2 are the shear force of the composite beams, N_1 and N_2 are the axial force of the composite beams, θ_1 and θ_2 are the rotation of the composite beams. Subscripts 1 and 2 denote the first and second story, respectively.

Fig. 28 compares the theoretical values (simplified calculation and FE modelling) with experimental values. For specimen SF-1, the calculation is lower than the experimental values and simulation results. The errors between the theoretical and measured values are less than 8.10%. For specimen SF-2, the calculation is lower than the experimental and simulation results for most cases, with a

maximum error of 8.14%. Therefore, the method can effectively reflect the vertical collapse resistance of composite frame.

(a) Specimens SF-1
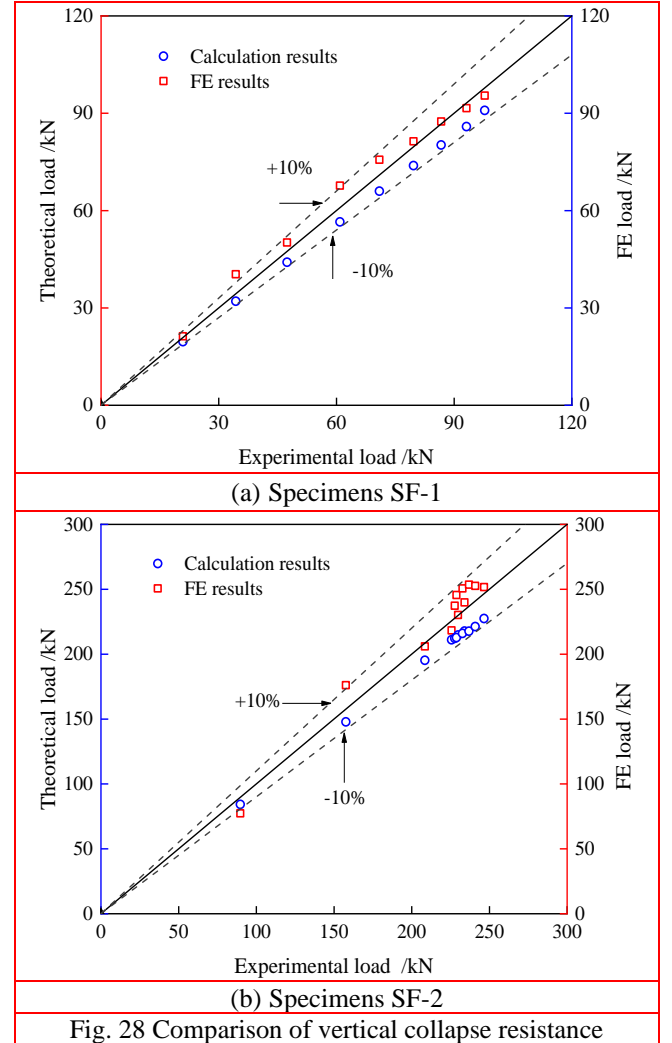

(b) Specimens SF-2

Fig. 28 Comparison of vertical collapse resistance

6 Conclusions

This study examines the progressive collapse behavior of two frame specimens under different column removal scenarios, yielding the following key findings:

•In the corner column removal scenario, deformation primarily localized in the failure span. Conversely, in the middle column removal scenario, varying degrees of failure occurred in both the left and right composite beams. For both scenarios, collapse initiation was triggered by the fracture of steel beam.

• As anticipated, the collapse resistance for the middle column removal scenario surpassed that of the corner column removal scenario. This can be attributed to the formation of a catenary mechanism formed in adjacent beams connected to the failure column in the middle column removal scenario, in addition to the flexural mechanism.

• Upper beams exhibited a more significant contribution

to resistance during the large deformation stage compared to lower beams. Horizontal reaction forces in middle column removal scenario exceeded those in the corner column removal scenario. The horizontal tie force of surrounding members exerted a notable impact on the remaining structure.

• Composite slabs significantly enhanced the collapse resistance of composite frame during large deformation stage. Additionally, the horizontal boundary constraint dramatically improved the collapse resistance of specimen SF-2. The column load ratio exhibited a limited effect on collapse resistance.

• The simplified theoretical method effectively evaluated vertical collapse resistance of composite frames at small deformation stage. For specimen SF-1 and SF-2, the discrepancy between the calculated and experimental values was 8.10% and 8.14% respectively.

Acknowledgements

References

Adam, J.M., Buitrago, M., Bertolesi, E. (2020), "Dynamic performance of a real-scale reinforced concrete building test under a corner-column failure scenario", *Eng. Struct.*, **210**, 110414. https://doi.org/10.1016/j.engstruct.2020.110414.

Adam, J.M., Parisi, F., Sagaseta, J., and Lu X.Z. (2018), "Research and practice on progressive collapse and robustness of building structures in the 21st century", *Eng. Struct.*, **173**, 122-149. https://doi.org/10.1016/j.engstruct.2018.06.082.

Almusallam, T.H., Al-Salloum, Y, Ngo, T.D., and Mendis P. (2017), "Experimental investigation of progressive collapse potential of ordinary and special moment-resisting reinforced concrete frames", *Mater Struct.*, **50**(2), 1–16. https://doi.org/10.1617/s11527-017-1014-x.

Almusallam, T.H., Elsanadedy, H.M., Al-Salloum, Y., and Siddiqui, N.A. (2018), "Experimental investigation on vulnerability of precast RC beam-column joints to progressive collapse", *KSCE J Civ Eng.*, **22**(10), 3995-4010. https://doi.org/10.1007/s12205-018-1518-0.

Al-Salloum, Y., Alrubaidi, M.A., Elsanadedy, H.M., and Almusallam, T. (2018), "Strengthening of precast RC beam-column connections for progressive collapse mitigation using bolted steel plates", *Eng. Struct.*, **161**, 146-160. https://doi.org/10.1016/j.engstruct.2018.02.009.

ASCE/SEI (2010), *Minimum design loads for buildings and other structures*. American Society of Civil Engineers, Washington DC, USA.

Campione, G. (2021), "Effect of progressive collapse of central column on the push-down response of two-span beam-column substructures", *Eng. Struct.*, **248**, 113119. https://doi.org/10.1016/j.engstruct.2021.113119.

CECS 392-2021(2021), *Standard for anti-collapse design of building structures*. China Planning Press, Beijing, China.

Chen, K., and Tan, K.H. (2020), "Structural behavior of composite moment-resisting joints under column-removal scenario". *J. Struct. Eng.*, **146**(3), 04019226. https://doi.org/10.1061/(ASCE)ST. 1943-541X. 0002518.

Demonceau, J.F., Jaspart, J.P. (2010), "Experimental test simulating a column loss in a composite frame", *Adv Steel Constr*, **6**(3), 891-913. https://doi.org/10.1142/S0578563410002166.

Diao, M.Z., Li, Y., Guan, H., Lu, X.Z., and Gilbert, B.P. (2020), "Influence of horizontal restraints on the behavior of vertical disproportionate collapse of RC moment frames", *Eng Fail Anal.*, **109**, 104324. https://doi.org/10.1016/j.engfailanal.2019.104324.

DoD (Department of Defense) (2016), *Design of buildings to resist progressive collapse*. Unified facilities criteria (UFC). Washington DC, USA.

Esmaeily, A., Xiao, Y. (2005), "Behavior of reinforced concrete columns under variable axial loads: analysis", *ACI Struct J.*, **102**(5), 736-744. https://doi.org/ 10.1109/ICMENS.2004.1509040.

Gao, S., Guo, L.H., Zhang, Z. (2021), "Anti-collapse performance of composite frame with special-shaped MCFST columns", *Eng. Struct.*, **245**, 112917. https://doi.org/10.1016/j.engstruct.2021.112917.

Gao, S., Xu, M., Fu, F., and Guo, L.H. (2019), "Performance of bolted steel-beam to CFST-column joints using stiffened angles in column-removal scenario", *J. Constr. Steel Res.*, **159**, 459-475. https://doi.org/10.1016/j.jcsr.2019.05.011.

GB228−2002 (2002), *Metallic materials Tensile testing Method of test at ambient temperature*. China Standard Press, Beijing, China.

GB50010-2010 (2010), *Code for design of concrete structures*. Ministry of Construction of China, Beijing, China.

Gruben, G., Fagerholt, E., Hopperatad, O.S., and Børvik, T. (2011), "Fracture characteristics of a cold-rolled dual-phase steel", *Eur J Mech A-solid.*, **30**(3), 204-218. https://doi.org/10.1016/j.euromechsol.2011.01.004.

GSA (General Service Administration) (2013), *Alternate path analysis & design guidelines for progressive collapse resistance*, General Services Administration, Washington (DC), USA.

Han, L.H. (2016), *Concrete filled steel tubular structures -Theory and practice* (3th edition), Science Press, Beijing, China.

Kang, S.B., Tan, K.H., Liu, H.Y., Zhou, X.H., and Yang, B. (2017), "Effect of boundary conditions on the behaviour of composite frames against progressive collapse", *J. Constr. Steel Res.*, **138**, 150-167. https://doi.org/10.1016/j.jcsr.2017.07.005.

Kong, D.Y., Yang, B., Elchalakani, M., Chen, K., and Ren, L.M. (2020), "Progressive collapse resistance of 3D composite slab system subjected to internal column removal: Experimental and numerical simulation", *J. Constr. Steel Res.*, **172**, 106208. https://doi.org/10.1016/j.jcsr.2020.106208.

Lew, H.S., Main, J.A., Robert, S.D., Sadek, F., and Chiarito, V.P. (2013), "Performance of steel moment connections under a column removal scenario. I: Experiments", *J. Struct. Eng.*, **139**(1), 98–107. https://doi.org/10.1061/(ASCE)ST.1943-541X.0000618.

Lu, X.Z., Lin, K.Q., Li, Y., Guan, H., Ren, P.Q. and Zhou, Y.L. (2017), "Experimental investigation of RC beam-slab substructures against progressive collapse subject to an edge-column removal scenario", *Eng. Struct.*, **149**, 91-103. https://doi.org/10.1016/j.engstruct.2016.07.039.

Lu, X.Z., Zhang, L., Lin, K.Q., and Li, Y. (2019), "Improvement to composite frame systems for seismic and progressive collapse resistance", *Eng. Struct.*, **186**, 227-242. https://doi.org/10.1016/j.engstruct.2019.02.006.

Ma, F., Gilbert, B.P., Guan, H., Lu X.Z., and Li, Y. (2019), "Experimental study on the progressive collapse behavior of RC flat plate substructures subjected to corner column removal scenarios", *Eng. Struct.*, **180**, 728–741. https://doi.org/10.1016/

j.engstruct. 2020.110299.

Meng, B., Li, L.D., Zhong, W.H., Tan, Z. and Zheng, Y.H. (2021), "Anti-collapse performance analysis of unequal span steel–concrete composite substructures", *Steel Compos. Struct*., **39**(4), 383-399. https://doi.org/10.12989/scs.2021.39.4.000.

Pham, A.T., Lim, N.S., Tan, K.H. (2017), "Investigations of tensile membrane action in beam-slab systems under progressive collapse subject to different loading configurations and boundary conditions", *Eng. Struct.*, **150,** 520–536. https://doi.org/10.1016/j.engstruct.2017.07.060.

Qian, K., Lan, X., Li, Z., Li, Y., and Fu, F. (2020), "Progressive collapse resistance of two-story seismic configured steel sub-frames using welded connections", *J. Constr. Steel Res.* **170**, 106117. https://doi.org/10.1016/j.jcsr.2020.106117.

Wang, J.J., Wang, W., Bao, Y.H., and Lehman, D. (2019), "Full-scale test of a steel moment-resisting frame with composite slab under a penultimate edge column removal scenario", *J. Constr. Steel Res.*, **162**, 1-13. https://doi.org/10.1016/j.jcsr. 2019.105717.

Wang, J.X., Yang, Y., Xian, W., and Li, Q.Y. (2020), "Progressive collapse mechanism analysis of concrete-filled square steel tubular column to steel beam joint with bolted-welded hybrid connection", *Int J Steel Struct*, **20**(5), 1618-1635. https://doi.org /10.1007/s13296-020-00397-3.

Wang J.X., Shen Y.J., Gao S. and Wang W.D., (2022), "Anti-collapse performance of concrete-filled steel tubular composite frame with assembled tensile steel brace under middle column removal", *Eng. Struct.*, **266**, 114635. https://doi.org/10.1016/j.engstruct.2022.114635.

Wang, W., Fang, C., Qin, X., Chen, Y.Y., and Li, B. (2016), "Performance of practical beam-to-SHS column connections against progressive collapse", *Eng. Struct.*, **106,** 332-347. https://doi.org/10.1016/j.engstruct.2015.10.040.

Wang, W.D., Zheng, L., Li, H.W. (2020), "Experimental investigation of composite joints with concrete-filled steel tubular column under column removal scenario", *Eng. Struct.*, **219**, 110956. https://doi.org/10.1016/j.engstruct.2020.110956.

Yang, B., Tan, K.H., Xiong, G., and Nie, S.D. (2016), "Experimental study about composite frames under an internal column-removal scenario", *J. Constr. Steel Res.*, **121**, 341-351. https://doi.org/10.1016/j.jcsr.2016.03.001.

Yang, X.J., Lin. F., and Gu. X.L. (2021), "Experimental study on a novel method to improve progressive collapse resistance of RC frames using locally debonded rebars", *J. Struct. Eng.*, **41**, 102428. https://doi.org/10.1016/j.jobe.2021.102428.

Zandonini, R., Baldassino, N., Freddi, F., and Roversoa, G. (2019), "Steel-concrete frames under the column loss scenario: An experimental study", *J. Constr. Steel Res.*, **162**, 105527.1-105527.21. https://doi.org/10.1016/j.jcsr.2019.02.036.

Zhong, W.H., Tan Z., Tian, L.M., Meng, B., and Zheng, Y.H. (2020), "Collapse resistance of composite beam-column assemblies with unequal spans under an internal column-removal scenario", *Eng. Struct.*, **206**, 110143. https://doi.org/10.1016/j.engstruct.2019.110143.

Zhu, Y.F., Chen, C.H., Huang, Y., Huang, Z.H., Yao, Y., and Keer, L.M. (2021), "Component-based model for posttensioned steel connections against progressive collapse", *Steel Compos. Struct.*, **40**(4), 481-493. https://doi.org/10.12989/scs. 2021.40.4.481.